catalysts

MDPI

Article

Spray-Dried Ni Catalysts with Tailored Properties for CO_2 Methanation

Bjarne Kreitz [1,*,†], Aurina Martínez Arias [2,†], Jan Martin [1], Alfred P. Weber [2] and Thomas Turek [1]

1 Institute of Chemical and Electrochemical Process Engineering, Clausthal University of Technology, Leibnizstr., 17, 38678 Clausthal-Zellerfeld, Germany; martin@icvt.tu-clausthal.de (J.M); turek@icvt.tu-clausthal.de (T.T.)

2 Institute of Particle Technology, Clausthal University of Technology, Leibnizstr., 19, 38678 Clausthal-Zellerfeld, Germany; aurina.martinez.arias@tu-clausthal.de (A.M.A.); weber@mvt.tu-clausthal.de (A.P.W.)

* Correspondence: kreitz@icvt.tu-clausthal.de; Tel.: +49-(53)2372-2473

† These authors contributed equally to this work.

Received: 26 October 2020; Accepted: 19 November 2020; Published: 2 December 2020

Abstract: A catalyst production method that enables the independent tailoring of the structural properties of the catalyst, such as pore size, metal particle size, metal loading or surface area, allows to increase the efficiency of a catalytic process. Such tailoring can help to make the valorization of CO_2 into synthetic fuels on Ni catalysts competitive to conventional fossil fuel production. In this work, a new spray-drying method was used to produce Ni catalysts supported on SiO_2 and Al_2O_3 nanoparticles with tunable properties. The influence of the primary particle size of the support, different metal loadings, and heat treatments were applied to investigate the potential to tailor the properties of catalysts. The catalysts were examined with physical and chemical characterization methods, including X-ray diffraction, temperature-programmed reduction, and chemisorption. A temperature-scanning technique was applied to screen the catalysts for CO_2 methanation. With the spray-drying method presented here, well-organized porous spherical nanoparticles of highly dispersed NiO nanoparticles supported on silica with tunable properties were produced and characterized. Moreover, the pore size, metal particle size, and metal loading can be controlled independently, which allows to produce catalyst particles with the desired properties. Ni/SiO_2 catalysts with surface areas of up to 40 $m^2\,g^{-1}$ with Ni crystals in the range of 4 nm were produced, which exhibited a high activity for the CO_2 methanation.

Keywords: spray-drying; Ni catalysts; CO_2 methanation; temperature-scanning reactor; aerosol synthesis

1. Introduction

Highly dispersed Ni nanoparticles supported on well-organized porous structures are promising catalysts for several applications such as steam and dry reforming of methane [1,2] and ethane [3,4], and methanation of CO [5,6] and CO_2 [7,8]. Especially the CO_2 methanation, which is part of the power-to-gas process, is becoming more important to tackle the needs for a sustainable natural gas economy. The dynamic operation of the CO_2 methanation in flexible load scenarios imposes challenges on the catalyst to perform well, even under drastic concentration and temperature variations [9–11]. For the improvement of the CO_2 methanation process and the other mentioned processes, it is, therefore, necessary to produce catalysts with long-term stability, sintering- and coking resistance as well as high activity and selectivity towards desired products. These properties are influenced on the microscale by

the size of the metal crystals, the pore size, and the metal/support interaction. Hence, in the production of the catalysts, it is of great interest to tailor the catalyst and the support to meet the specifications of the task at hand. Various ceramic carriers are investigated for CO_2 methanation, such as γ-Al_2O_3, SiO_2, TiO_2, CeO_2, and ZrO_2 [8,12–14]. Carriers with basic surface properties like Al_2O_3 and CeO_2 show a high CO_2 methanation activity due to the interaction of CO_2 with basic adsorption sites [15]. Ni supported on structured mesoporous SiO_2 nanoparticles also has a high activity and SiO_2 supports have the potential to be tailored [16].

In recent literature, several production methods for Ni/SiO_2 catalysts have been tested, aiming to influence the pore system and Ni crystal size. Aziz et al. [16] prepared mesostructured silica nanoparticles using a sol-gel method. These showed approximately 50 % higher activity compared to classical impregnated Ni/SiO_2 catalysts. A mesoporous silica molecular sieve with a highly accessible pore system was prepared by Chen et al. [17], which proved to be a more active support than amorphous SiO_2. By using the ammonia evaporation method and colloidal silica as starting material, Ye et al. [18] were able to increase the surface area of the SiO_2 support by 140 $m^2\,g^{-1}$ compared to commercial carriers and to decrease the Ni crystal size. Furthermore, Zhu et al. [19] prepared a bimodal pore structure with pores in the range of 5 to 50 nm by impregnation of SiO_2 nanoparticles.

Most of the catalysts are produced by impregnation methods of the different support materials [19–22], co-precipitation [23], so-gel [16], and flame synthesis [24,25]. The first three of these methods are usually batch processes and require various time-consuming steps. Moreover, there is a loading limitation for impregnation methods, which is in the range of 30 % depending on the pore volume, as well as a direct correlation between the pore size and the metal particle size [26–28]. In addition, the metal particle size is dependent on the metal loading. Usually, metal dispersion decreases with increasing metal loading. Flame synthesis is a fast and single-step process that does not require a post-heat treatment of the particles as the thermal decomposition occurs directly in the flame due to the high temperatures. However, the high cost of the precursor and the difficulties of producing porous materials are the drawbacks of this method, which still needs to be improved [29]. Another possible way of producing catalysts is the spray-drying method. It is a simple, efficient, continuous, fast, and easily scaleable process to synthesize nanoparticles in a few preparation steps [30]. In previous work, Martínez and Weber [31] presented a method for synthesizing highly dispersed Co_3O_4 nanoparticles supported on silica with tunable properties such as pore size, surface area, metal particle size, and metal loading by spray-drying a colloidal silica suspension with dissolved metal nitrate. Furthermore, they show how to control the pore size and the metal particle size independently, as well as a design guide to determine the metal particle size for a certain metal concentration per surface area.

Ni/SiO_2 and Ni/γ-Al_2O_3 catalysts are produced in this study with the spray-drying process presented by Martínez and Weber [31]. Variation in the primary particle size of the silica, Ni loading, and thermal treatment are studied to provide a design guide for the catalytic materials. Catalysts are examined with physical and chemical characterization techniques such as X-ray diffraction, temperature-programmed reduction, and chemisorption. The CO_2 methanation is used as a test reaction to investigate the activity of the produced catalysts. To enable a quick screening of the materials, a temperature-scanning technique, developed by Wojciechowski and Asprey [32,33] is applied, which was successfully used to investigate the kinetics of CO oxidation [34] and ammonia synthesis [35]. The results from this work will provide a guideline to vary catalysts properties such as pore size, metal particle size, and the metal/support interaction. This tailoring of the catalysts enables us to investigate the structure-activity relation for the CO_2 methanation on Ni/SiO_2 catalysts.

2. Results and Discussion

2.1. Morphological Examination

The particles synthesized in this work, referred to as building blocks (BB), were produced from a suspension of water, nickel nitrate, and colloidal nanoparticle suspension (SiO_2 or Al_2O_3). The prepared suspension was atomized and sprayed into a tube furnace operated at 673 K to evaporate the solvent and to decompose most of the $Ni(NO_3)_2$ to NiO, leading to the formation of a NiO/SiO_2 nanoparticle. A detailed scheme of the setup can be found in previous work [31]. During the drying in the tube furnace, the evaporation of the solvent in the droplets initiated a self-assembly process leading to spherical dry particles formed by several small single nanoparticles. In this study, BB formed by two different supports, SiO_2 with two different primary particle sizes (8 and 20 nm), here named as BB(8) and BB(20) and Al_2O_3 with a primary particle size of 50 nm (BB(Al_2O_3)), using two different nickel loadings of 10 and 20 wt% were produced. The nickel loading in the BB can easily be adjusted by adding different nickel nitrate amounts to the prepared suspension before the spray-drying process. Continuously synthesized nanoparticles were collected on a filter and heat-treated in a muffle oven at two different temperatures of 673 K and 973 K to adjust the NiO nanoparticle size. Temperatures higher than 973 K were not used in this work to avoid sintering of SiO_2 nanoparticles, which is discussed in more detail in the supporting information (SI) (see Figures S1 and S2). A tree summarizing the produced samples is provided in Figure 1.

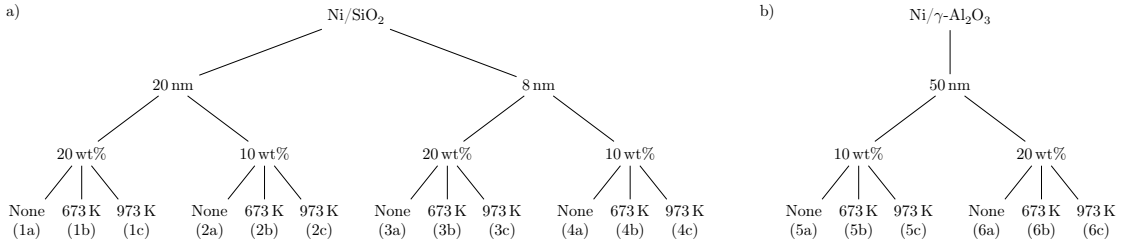

Figure 1. Tree for the production of the (**a**) Ni/SiO_2 and (**b**) Ni/γ-Al_2O_3 catalysts. The first node is the size of the primary particles (SiO_2 or Al_2O_3) of the support in the colloidal suspension, the second node is the Ni loading, and the third child node is the temperature of the thermal treatment after the synthesis. The names of the samples are placed in parentheses.

Figure 2 shows the SEM and TEM micrographs of BB(20) and BB(Al_2O_3) with 20 wt% of Ni after production (c and d), and after the heat treatment in a muffle oven for 4 h at 973 K (a, b, e, and f). The SEM images reveal that the spray-drying method produces a broad particle size distribution of spherical nanoparticles with diameters up to 300 nm. Each of these agglomerates consists of many tightly packed single SiO_2 nanoparticles with a size of 20 nm (for BB(20)) and well-distributed NiO nanoparticles (darker dots), which can be seen in Figure 2c,e. TEM images with BB(8) and BB(45) show the same behavior (see Figure S3). Furthermore, it can be observed that the size of the NiO nanoparticles grew during the heat treatment due to the sintering effect. BB(Al_2O_3) are also compact spheres formed by single Al_2O_3 nanoparticles. However, for BB(Al_2O_3), it is not possible to observe clusters of NiO crystals (see Figure 2d,f).

2.2. Elemental Analysis

The catalysts were produced in a single batch and a part of this batch was calcined at 673 K and 973 K. That is why the samples with one BB and nominal loading, e.g., BB(20) with 10 wt%, have the same Ni content (13 wt%) and traces of Na (0.003 wt%) and K (0.019 wt%) for the three different calcination temperatures. K and Na can affect the activity of the silica and alumina catalysts [36,37]. Traces of Na and K can originate from the Ni nitrate or the silica suspension and the presence of Na can create basic sites on the support. Studies show that Na enhances the CO_2 methanation activity of Ni/SiO_2 catalysts [37], whereas it increases the CO selectivity in Ni/Al_2O_3 catalysts [38].

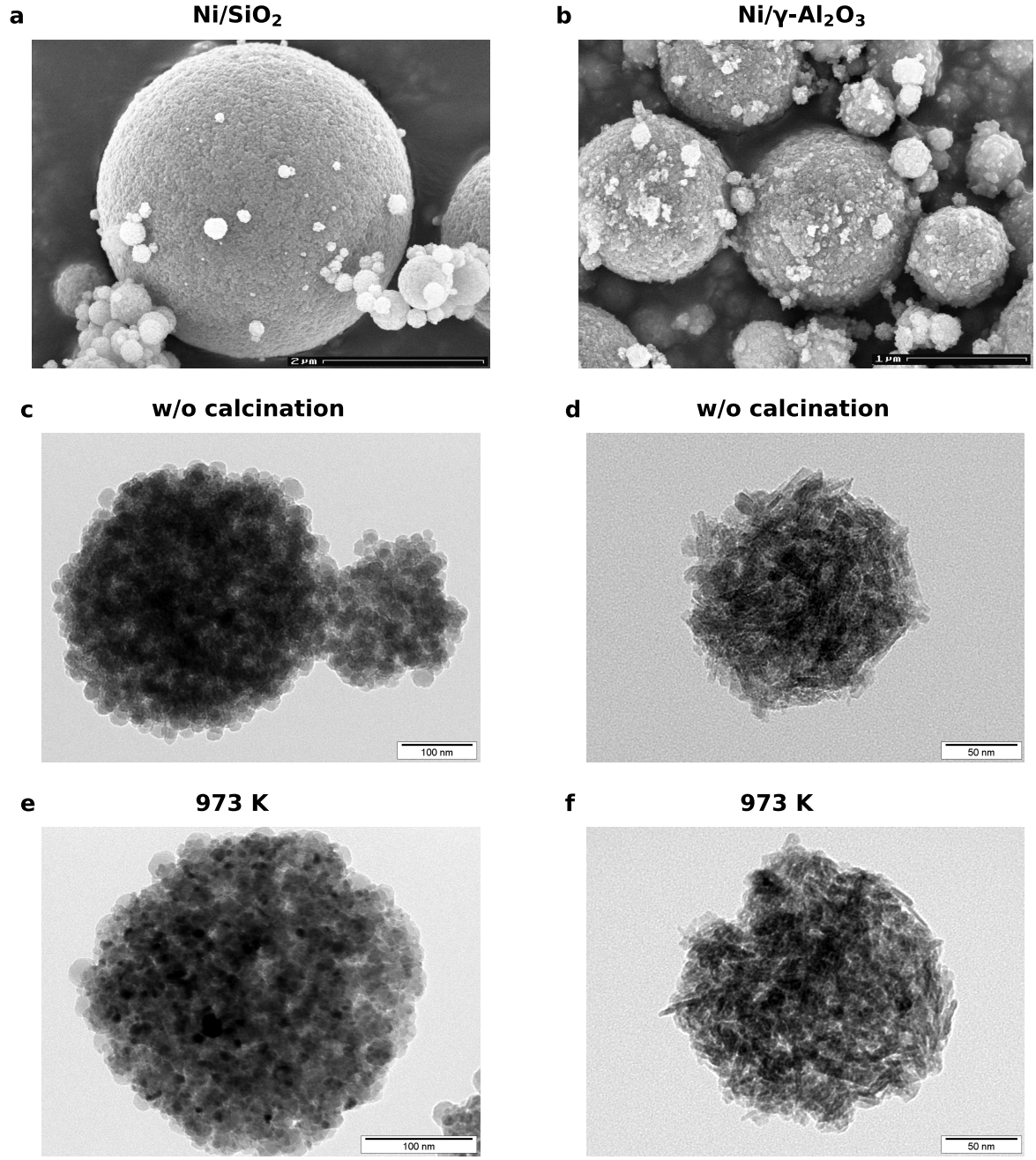

Figure 2. SEM images of the (**a**) BB(20) and (**b**) BB(Al_2O_3) with a Ni loading of 20 wt%. TEM micrographs of (**c**) BB(20) and BB(Al_2O_3) (**d**) after production (without (w/o) calcination). (**e**) BB(20) and (**f**) BB(Al_2O_3) after calcination at 973 K for 4 h.

The measured Ni content in the silica catalysts is always higher than the value, which was initially provided in the atomizer (see Table 1). For the alumina catalysts, the amount of Ni is lower (see Table 2). The amount of potassium in all catalyst samples is in the range of 0.02 wt% and thus negligible. The concentration of Na varies in the different samples. A negligible amount of Na is obtained for the BB(20), but for the catalysts with BB(8) and BB(Al_2O_3), the amount of Na is in the range of 0.1 wt%. Catalysts produced with BB(20) show a lower Na concentration compared to the ones produced from BB(8). The influence of basic sites will be further investigated with CO_2 temperature-programmed desorption (TPD) experiments.

Table 1. Summary of the characterization results for all Ni/SiO_2 catalysts. The naming convention applied in this work is provided in Figure 1. The samples that were not calcined (1a, 2a, 3a, 4a) loose mass during the reduction because of the decomposition of remaining nitrates. This mass loss was measured with a thermogravimetric analysis (see Table S1) and accounted for in the evaluation.

Property	Unit	1a	1b	1c	2a	2b	2c	3a	3b	3c	4a	4b	4c	Method
Surface area	$m^2\,g^{-1}$	-	110	96	-	111	103	-	184	153	-	199	181	BET
Pore volume	$mm^3\,g^{-1}$	-	281	269	-	290	272	-	357	334	-	398	375	BJH
Average pore size	nm	-	9.0	9.3	-	9.1	8.6	-	6.4	6.6	-	6.7	6.6	BJH
Ni loading	wt%	20.9	20.9	20.9	13.0	13.0	13.0	23.1	23.1	23.1	12.2	12.2	12.2	ICP-OES
Na content	wt%	0.01	0.01	0.01	<0.003	<0.003	<0.003	0.12	0.12	0.12	0.15	0.15	0.15	ICP-OES
K content	wt%	0.018	0.018	0.018	0.019	0.019	0.019	0.014	0.014	0.014	0.011	0.011	0.011	ICP-OES
H_2 uptake	$\mu mol\,g^{-1}$	402	181	93	254	171	58	460	271	110	324	205	95	H_2 chemisorption
Metal surface area	$m^2\,g^{-1}$	34.3	16.3	8.9	28.1	17.6	8.4	40.5	23.8	12.0	34.6	21.1	11.3	H_2 chemisorption
Average Ni crystal size	nm	4.1 (4.5)	8.6 (6.8)	15.9 (8.3)	3.1 (3.2)	5.0 (4.7)	10.4 (5.4)	3.9 (4.3)	6.5 (5.1)	12.9 (5.9)	2.4 (2.0)	3.9 (2.5)	7.3 (2.8)	H_2 chemisorption (XRD)
Ni dispersion	%	24.6	11.7	6.3	32.4	20.2	9.7	26.2	15.4	7.8	42.4	25.9	13.9	H_2 chemisorption
Degree of reduction	%	91.9	87.0	82.7	70.8	76.6	53.9	89.2	89.2	71.4	73.5	76.3	66.2	O_2 chemisorption
CO_2 uptake	$\mu mol\,g^{-1}$	78.5	26.6	-	-	-	-	126.3	53.5	16.9	-	-	-	CO_2 chemisorption

Table 2. Summary of the characterization results for the $Ni/\gamma\text{-}Al_2O_3$ catalysts. It was not possible to determine the NiO size for the alumina catalysts with XRD because only $NiAl_2O_4$ was formed.

Property	Unit	5a	5b †	5c †	6a	6b	6c †	Method
Surface area	$m^2\,g^{-1}$	-	178	123	-	155	99	BET
Pore volume	$mm^3\,g^{-1}$	-	337	331	-	311	293	BJH
Average pore size	nm	-	5.9	8.0	-	6.4	8.7	BJH
Ni loading	wt%	9.0	9.0	9.0	15.1	15.1	15.1	ICP-OES
Na content	wt%	0.16	0.16	0.16	0.17	0.17	0.17	ICP-OES
K content	wt%	0.0055	0.0055	0.0055	0.0046	0.0046	0.0046	ICP-OES
H_2 uptake	$\mu mol\,g^{-1}$	7	-	-	143	69	-	H_2 chemisorption
Metal surface area	$m^2\,g^{-1}$	5.8	-	-	28.3	18.1	-	H_2 chemisorption
Average Ni crystal size	nm	14.5	-	-	2.9	4.5	-	H_2 chemisorption
Ni dispersion	%	7.1	-	-	34.7	22.3	-	H_2 chemisorption
Degree of reduction	%	9.6	-	-	39.6	29.8	-	O_2 chemisorption
CO_2 uptake	$\mu mol\,g^{-1}$	140.9	-	-	125.6	-	-	CO_2 chemisorption

† With the applied reduction method, it was not possible to reduce $NiAl_2O_4$, which did not allow for a proper determination of the H_2 adsorption capacity, because the detected amounts are too small.

2.3. Physisorption

The pore size distributions of BB(8), BB(20), BB(45), and BB(Al_2O_3) with 20 wt% Ni calcined at 673 K, are illustrated in Figure 3a. It can be observed that the average pore size increases with an increasing primary particle size of the silica. Smaller pores with a narrow size distribution are formed for smaller SiO_2 nanoparticles. On the other hand, the total pore volume increases as the size of the SiO_2 nanoparticles is decreased (see Table 1), which indicates that the porosity of the BB decreases with increasing the SiO_2 primary particle size. These results agree with the observations that the arrangement, or ordering ability of larger nanoparticles, is easier than the arrangement of smaller nanoparticles [31,39–41]. The pore size of BB(8), as well as the surface area and the total pore volume, is very similar to the pore size distribution of BB(Al_2O_3).

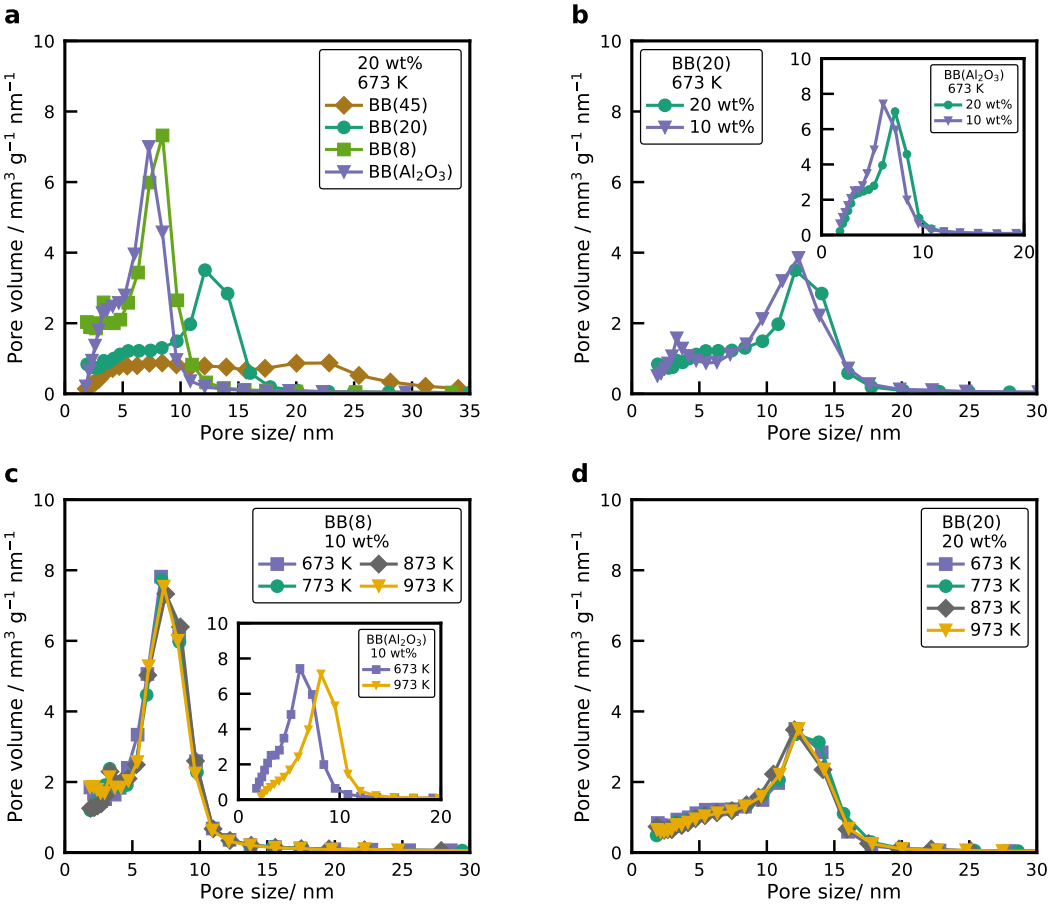

Figure 3. (**a**) Pore size distribution of BB(8), BB(20), BB(45), and BB(Al_2O_3) with 20 wt% of Ni, calcined at 673 K. (**b**) Pore size distribution of BB(20) and BB(Al_2O_3) (inset) with two different nickel loadings (10 and 20 wt%), calcined at 673 K. (**c**) Pore size distribution of BB(8) and BB(Al_2O_3) (inset) with 10 wt% of Ni calcined at different temperatures. (**d**) Pore size distribution of BB(20) with 20 wt% of Ni calcined at different temperatures.

Figure 3b shows the pore size distribution of BB(20) with two different nickel loadings. The pore size distribution of the BB is not affected by the different nickel loadings, whereas the total pore volume of the BB decreases with increasing Ni loading because the NiO nanoparticles occupy the free space. The same behavior was observed for a primary particle size of 8 nm with two different Ni loadings. This confirms that the final structure of the NiO/SiO_2 nanoparticles mainly depends on the primary particle size of the silica. This is contrary to catalysts produced via incipient wetness impregnation, where the pore size decreases with increasing Ni loading [26–28,42]. However, an increase in the nickel loading for BB(Al_2O_3) results in a small shift towards larger pores with lower total pore volume

(see inset Figure 3b and Table 2). For BB(Al_2O_3) the nickel reacts with the support and creates a new crystalline structure, consisting of crystalline $NiAl_2O_4$ as well as γ-Al_2O_3. The new crystalline structure induces morphological changes on the particle, which results in a different pore structure. With higher Ni loading the share of $NiAl_2O_4$ increases, which slightly changes the pore size distribution. The pore size distribution of BB(8) with 10 wt% Ni calcined at different temperatures is displayed in Figure 3c. It can be observed that the pore size distribution of the NiO/SiO_2 system does not change with increasing calcination temperature, while the size of the NiO nanoparticle increases. The same behavior is obtained for BB(20) with 20 wt% of Ni (see Figure 3d). However, for the BB(Al_2O_3), the pore size increases with higher calcination temperatures (see Figure 3c inset), which is due to the changes in the structure of the Al_2O_3 nanoparticles because of sintering (see Figure S2). The experimental results show that pore size distribution, total pore volume, and specific surface area of the BB can be easily adjusted by varying the SiO_2 primary particle size. For NiO nanoparticles supported on silica, there is no correlation between the pore size, the NiO nanoparticle size, and the nickel loading. These experiments agree with previous work from our group [31,41] for cobalt oxide nanoparticles supported on silica. However, further experiments have to be performed for BB(Al_2O_3) with different primary particle sizes. So far, it can observed that the pore size of BB(Al_2O_3) is influenced by the nickel loading and the different calcination temperatures.

2.4. XRD

The XRD patterns of BB(20) and BB(Al_2O_3) with 20 wt% Ni after production and after the heat treatment at different temperatures are illustrated in Figure 4. Higher calcination temperatures resulted in diffractograms with more pronounced reflections for the SiO_2 catalysts (see Figure 4a), which indicates that the NiO nanoparticle size increased due to sintering effects. The average size of the NiO nanoparticles was calculated from the Scherrer Equation (1) using the full-width at the half-maximum value of the peak with maximum intensity, which is the NiO(200) facet. The average NiO nanoparticle size of the different samples are plotted in Figure 5.

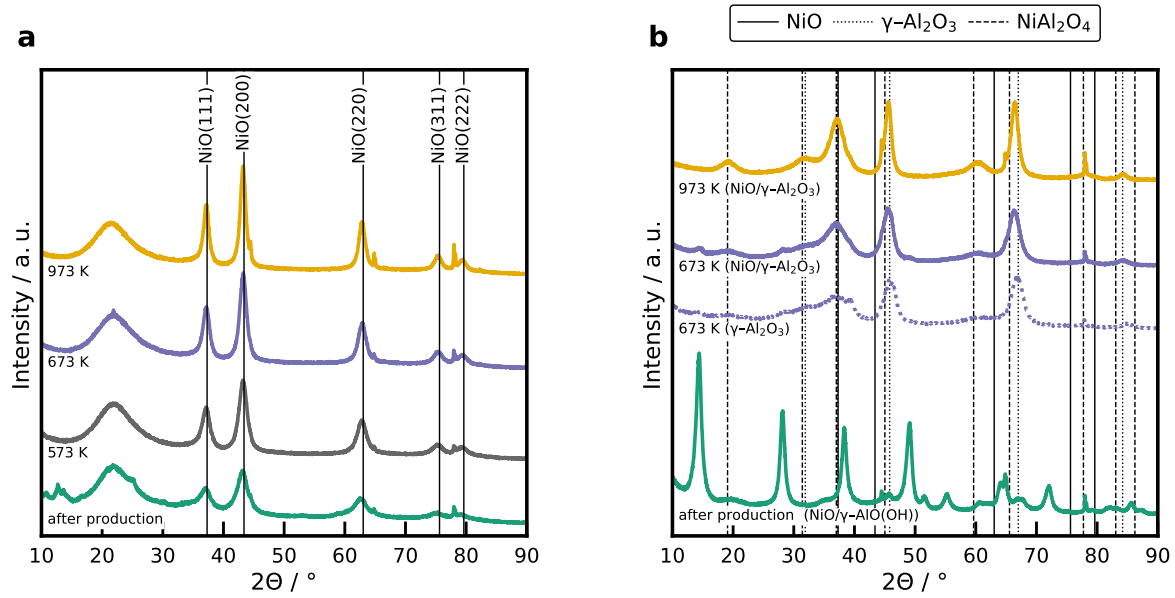

Figure 4. (**a**) XRD patterns of the 20 wt% Ni/SiO_2 catalyst with BB(20) after production, and after calcination at different temperatures. The broad reflection at $2\Theta = 22°$ is assigned to amorphous silica and the reflections at 38.2, 44.6, 65.0, 78.0, and 78.1° are caused by the Al sample holder. (**b**) XRD patterns of the 10 wt% Ni/Al_2O_3 catalyst after production, and after calcination at 673 K and 973 K for 4 h. Reflections for the boehmite structure obtained after production is provided in Figure S4a.

The XRD profiles of BB(Al_2O_3) with 20 wt% of Ni directly after production and heat treatment at two different temperatures are plotted in Figure 4b, as well as the XRD profile of BB(Al_2O_3) without Ni. Only Ni aluminate spinel structures were formed and no reflections corresponding to NiO nanoparticles were found, even for the low calcination temperature. Furthermore, it can be seen that there is a phase transition in the crystalline structure before and after calcination. A boehmite structure is formed for temperatures below 673 K, whereas for temperatures higher than 673 K, a phase transition to γ-Al_2O_3 and $NiAl_2O_4$ is observed (see Figure S4a). Increasing the nickel loading in BB(Al_2O_3) shifts the reflections towards smaller angles (see Figure S4b), which indicates a volume increase in the unit cell due to the incorporation of the bigger Ni atoms in the alumina spinel structure. With a Rietveld analysis, it was possible to simulate the XRD pattern assuming only γ-Al_2O_3 and $NiAl_2O_4$ and to derive the lattice constant of γ-Al_2O_3. The lattice constant as a function of the Ni loading is presented in Figure S4c. A higher nickel loading increases the lattice constant of the γ-Al_2O_3, which is reasonable as the ionic radius of Ni is higher than the ionic radius of Al [43]. Results from the Rietveld analysis agree well with reported literature values [44,45].

The sintering of metal oxide nanoparticles is known to be temperature- and size-dependent [46,47]. However, the sintering of metals can be affected by other factors such as melting point [48], the shape and composition of the nanoparticle [49], the interaction between the support and the metal [50], or the metal loading [50,51]. Especially the metal loading will have a large impact on the nanoparticle growth. For instance, for higher metal loadings, the ratio between the total mass of metal per surface area of the support (m_{Ni}/a_{SiO_2} ratio) increases, and thus, the metal particle size increases, e.g., BB(20) and 20 wt% Ni has a ratio of 2.0 mg m^{-2}, whereas for BB(20) and 10 wt% of Ni the ratio is 1.13 mg m^{-2}. Herein, the growth of the NiO nanoparticle as a function of the nickel loading inside the BB was investigated. Figure 5a shows the NiO nanoparticle size of BB(20) for the different nickel loadings, calcined at different temperatures. Increasing the nickel loading increases the size of the NiO nanoparticles for the same calcination temperature. For instance, for higher nickel loadings (e.g., 20 wt% of Ni in BB), the size of the NiO nanoparticles presents a stronger increase with the temperature, whereas for low nickel loadings (e.g., 5 wt% of Ni in BB), the growth of the NiO nanoparticles is very small. In any case, the size of the NiO nanoparticles increases linearly with increasing calcination temperature, which is in agreement with the experimental results of other groups [50,52].

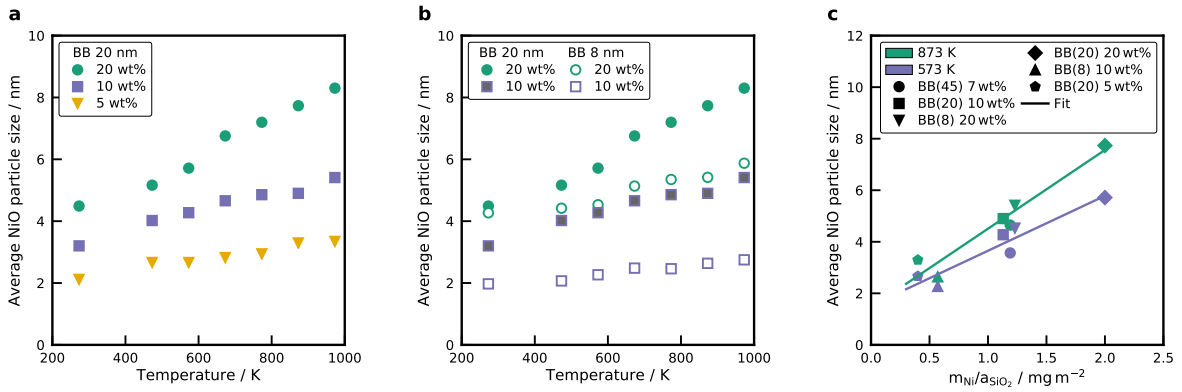

Figure 5. Average NiO nanoparticle size of the different samples calculated using the Scherrer equation Equation (1) for (**a**) BB(20) with different Ni loading, calcined at different temperatures and (**b**) comparison of BB(8) and BB(20) with two different Ni loadings at different calcination temperatures. (**c**) Average NiO crystal size in dependence of the m_{Ni}/a_{SiO_2} ratio for various catalysts with different SiO_2 primary particle sizes (8, 20 and 45 nm) and Ni loadings (5, 10 and 20 wt%) at two temperatures (see Table S2). A linear regression is displayed to illustrate the observed trend.

As mentioned before, the m_{Ni}/a_{SiO_2} ratio also plays an important role in the final size of the NiO nanoparticle. Thus, the BB formed with two different SiO_2 primary particle sizes (BB(8) and BB(20)) for two different nickel loadings (10 and 20 wt%) were compared to investigate the influence

of the size of the NiO nanoparticle as a function of the metal mass and absolute surface area of the support. Figure 5b shows the average NiO nanoparticle sizes of the different BB calcined at different temperatures. For BB formed with smaller SiO_2 primary particle size, smaller NiO nanoparticles result, compared to the BB formed with bigger SiO_2 nanoparticles at the same loading. Moreover, the size of the NiO nanoparticles was very similar for BB(20) with 10 wt% of Ni, compared to the NiO nanoparticle size of BB(8) and 20 wt%. Notice that for these two catalyst, the m_{Ni}/a_{SiO_2} ratio is very similar. BB(20) and 10 wt% Ni has a ratio of 1.13 mg m^{-2}, whereas for BB(8) and 20 wt% of Ni, the ratio is 1.23 mg m^{-2}, which explains the similar size of the NiO nanoparticles. The dependence of the m_{Ni}/a_{SiO_2} ratio on the NiO crystal size is clearly illustrated in Figure 5c. Notice that the NiO size for three different SiO_2 primary particle sizes and Ni loadings shows a linear increase in the NiO crystal size with increasing m_{Ni}/a_{SiO_2} ratio. As shown before, the NiO crystal size depends on the temperature, but the correlation between m_{Ni}/a_{SiO_2} ratio and average NiO crystal size stands to reason for all of the investigated temperatures. These results are in agreement with the work of Martínez and Weber [31] for Co_3O_4 nanoparticles supported on silica. However, the assumption that the same m_{Ni}/a_{SiO_2} ratio results in the same NiO nanoparticle size is only valid when the same materials are used (e.g different nickel loadings, silica nanoparticles with different sizes). Loosdrecht et al. [50] compared the results of the NiO nanoparticle size when the same nickel loading was distributed over two different supports (SiO_2 and TiO_2), while the specific surface area for both supports was kept constant. They observed that the size of the nickel oxide nanoparticles was different for the two supports due to the different behavior of nucleation and growth on the support. The linear regression in Figure 5c can be used as a design guide to tailor the NiO crystal size to a specific value by choosing the size of the primary particle and the temperature of the post-heat treatment.

All of the XRD patterns were reported for the calcined samples. Therefore, the determined crystal size refers to the NiO crystal. In order to determine the crystal size of Ni, the catalyst samples were reduced and passivated with synthetic air at room temperature using a pulse method [53]. Figure S5a shows the diffractogram of the Ni/SiO_2 catalyst formed using BB(20) with 20 wt%, calcined at 673 K) after calcination, while Figure S5b shows a diffractogram after reduction and passivation. It can be seen that large Ni reflections with broad low-intensity NiO reflections were obtained for the passivated sample. This allows to determine the Ni crystal size. The NiO crystal size determined from the NiO(111) reflection for the non-reduced catalyst with BB(20), 20 wt% calcined at 673 K is 6.8 nm. For the reduced and passivated catalyst, the Ni crystal size was calculated from the Ni(111) reflection and amounts to 6.9 nm. No change in the crystal size is determined upon reduction. Therefore, the values determined for NiO can be used as the size of the Ni crystals. Small-angle X-ray scattering (SAXS) measurements of this catalyst (see Figure S6) show a monomodal Ni particle size with a most frequent Ni crystal size of 7 nm, which fits the XRD results.

According to the experimental results presented above, it can be concluded that the size of the NiO nanoparticles can be controlled by varying the calcination temperature in a post-heat treatment after the synthesis of the BB. Furthermore, it can be seen that there is a dependence on the amount of nickel per surface area of the support (mass of nickel per surface of silica), which agrees well with the experimental results of Martínez and Weber [31]. This observation can be used as a design guide to synthesize metal oxide nanoparticles supported on spherical silica nanoparticles with defined metal nanoparticle size for a specific metal concentration per surface area of the support for a chosen calcination temperature. On the other hand, this design guide can not be applied for BB(Al_2O_3) with Ni as it was not possible to produce dispersed NiO nanoparticles on the Al_2O_3 surface due to the formation of $NiAl_2O_4$.

2.5. Adsorption and Degree of Reduction

H_2 adsorption was performed to determine the amount of active Ni sites. Active metal surface area, Ni crystal diameter and the dispersion were calculated using Equations (3) to (5). The adsorption capacity was determined from a volumetric isotherm with the back-extrapolation of the linear part

(see Figure S7). Results are summarized in Table 1 for SiO_2 and Table 2 for Al_2O_3. It is evident that the H_2 adsorption capacity is a strong function of the calcination temperature because of the XRD results. The highest H_2 uptake is always determined for the uncalcined samples. An increase in the calcination temperature increases the size of the Ni particles, as shown by the diffractograms, and reduces the active metal surface area. The catalyst with BB(8) and 20 wt% has a monolayer coverage of 460 µmol g^{-1}, which corresponds to a Ni surface area of 40 m^2 g^{-1} and a Ni crystal size of 3.9 nm. After calcination at 673 K this value decreases to 271 µmol g^{-1}, 23.8 m^2 g^{-1}, and the crystal size increases to 6.5 nm. The catalyst produced using BB(20) with 10 wt% has the smallest Ni crystal size of 2.4 nm and the highest dispersion of 42.4%. Particle sizes determined via H2 adsorption and XRD are in reasonable agreement for the uncalcined samples and those after calcination at 673 K. However, the crystal size calculated from H_2 adsorption for the samples with a calcination temperature of 973 K deviates significantly.

After calcination at high temperatures, the samples become harder to reduce, seen by the degree of reduction (*DOR*). The *DOR* for BB(20) with 20 wt% of Ni was 91.9% when reduced in pure H_2 at 723 K (10 K min^{-1}) for 1 h, whereas after calcination at 673 K this value drops to 87% and to 82.7% after calcination at 973 K. Ni particle sizes measured with XRD indicate smaller Ni crystals, which interact strongly with the support and cannot be entirely reduced. Catalysts with a loading of 10 wt% are even more difficult to reduce after calcination at 973 K compared to those with a higher loading and show a *DOR* of only 54% (BB(20)) and 66% (BB(8)). A higher Ni loading leads to bigger NiO crystals, which are easier to reduce [54,55].

2.6. Temperature-Programmed Reduction

Temperature-programmed reduction (TPR) profiles of all catalysts are displayed in Figure 6a. The NiO reference has a single reduction peak with a maximum at 650 K and a long tailing to higher temperatures. When comparing TPR profiles of Ni/SiO_2 catalysts with the literature, it has to be kept in mind that water in the gas phase can significantly alter the reduction profiles of silica catalysts [56]. High water concentrations in the gas phase retard the reduction due to the formation of surface nickel silicates, which cover the NiO crystals and are more challenging to reduce [56]. The reduction profile of the silica catalysts show the same behavior for different calcination temperatures. Therefore, the catalyst with BB(20) and 20 wt% (Figure 6a top) is explained in greater detail. TPR profiles of the catalysts can be deconvoluted by fitting Gaussian profiles to the recorded spectra, which is illustrated for this catalyst after calcination at 673 K in Figure 6b (top) and 973 K in Figure 6b (bottom). Silica catalysts with a metal loading of 20 wt% show four discernible overlapping peaks, whereas the 10 wt% catalysts have five.

A sharp peak with a maximum at 520 K is observed for the uncalcined sample, which corresponds to the decomposition of remaining nitrates. This is also evidenced by the recorded mass spectrometer (MS) signal and displayed in the SI (see Figure S8). The short residence time of the catalyst (1.6 s) in the tubular furnace at 673 K is not sufficient to decompose all the nitrates. After thermal pretreatment at 673 K or 973 K, the first peak diminishes, and three overlapping peaks remain visible. The decomposition peak for the catalyst with BB(20), 10 wt%, and without calcination is shifted to a higher temperature of 540 K. For the 10 wt% samples, a second low-temperature peak is observed at a temperature of 538 K. This reduction peak can be attributed to Ni_2O_3, which is formed by the decomposition of $Ni(NO_3)_2$ in H_2 atmosphere [57]. Mile et al. [54] reported that Ni_2O_3 is reduced at temperatures of 523 K. The main reduction peak for the 20 wt% catalysts occurs at a temperature of 600 K for BB(20) with 20 wt% and at 630 K for the BB(8) with the same loading. For the lower loadings, this is shifted to higher temperatures of 700 K. Smaller NiO nanoparticles are formed with a lower Ni loading, and these small NiO particles were harder to reduce than big NiO crystals [54,58]. A high-temperature shoulder is observed with a maximum temperature of 730 K, which can be associated either with particles, in which SiO_4 is incorporated into the NiO lattice [59], or with 1:1 Ni phyllosilicates [55,58,60]. SiO_4 retards the reduction of the bulk NiO and causes a higher temperature

peak at 730 K. The Ni phyllosilicates form a layered structure, where the Ni^{2+} ions were in an octahedral configuration [55,58,60]. Louis et al. [58] reported a formula of $Ni_3Si_2O_5(OH)_4$ for a 1:1 phyllosilicate, which is also known as antigorite according to Coenen [61]. The reduction peak of these 1:1 phyllosilicates is in the range of 773 K to 973 K. With the characterization methods used in this work, it was not possible to precisely identify the formed silicate, and the comparison with literature was not definite because of the retarding effect of gaseous water, which can induce the formation of surface silicates during the reduction [56].

After calcination at 673 K for 4 h the decomposition of the precursor is complete, and three peaks remain visible at 580 K, 650 K, and 800 K. The low-temperature shoulder is in the same temperature range as the reduction of Ni_2O_3 [54,58]. The reduction peak at 630 K is in line with the NiO reference (650 K) and thus indicating the reduction of NiO, which interacts only to a small extent with the silica surface, also referred to as bulk NiO. Literature values for the reduction of bulk NiO on silica are in the range of 673 K [54,58]. The high-temperature peak is extended to higher temperatures and is a result of the silicate formation.

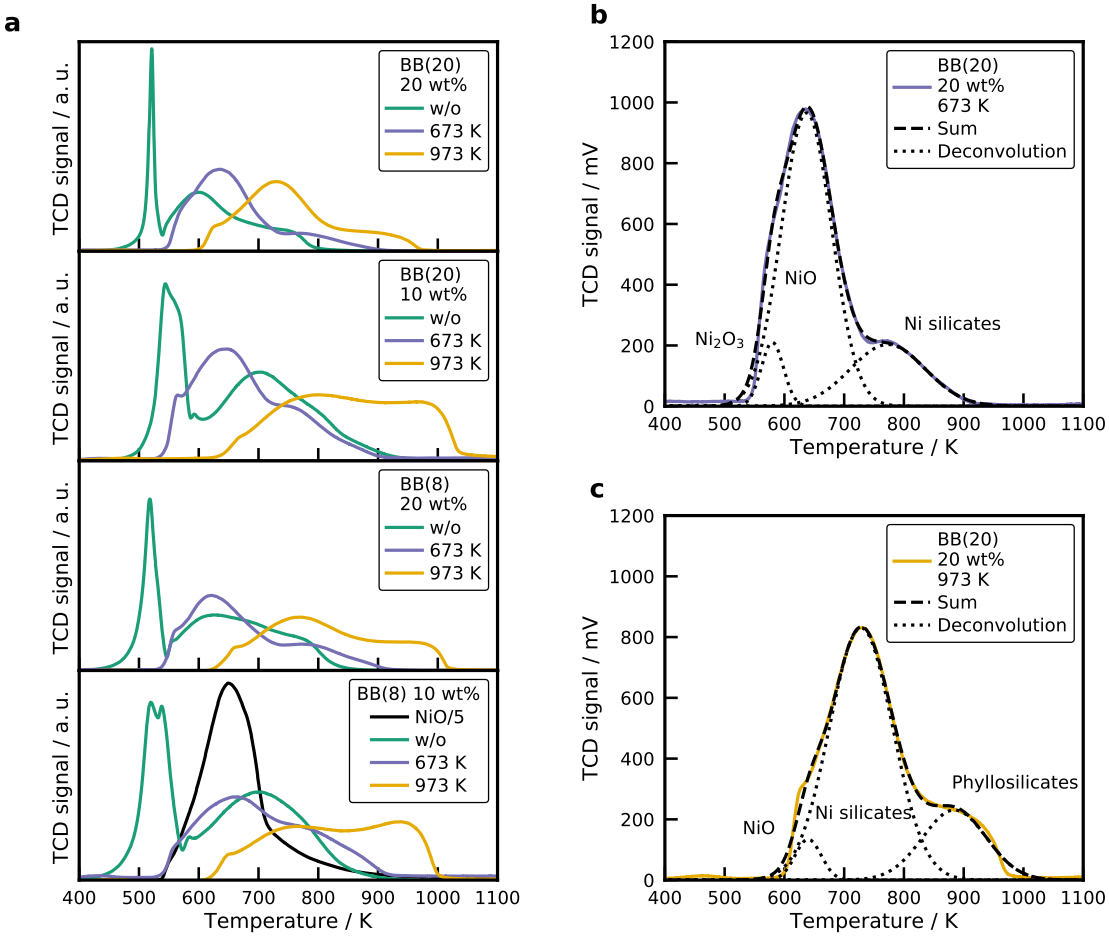

Figure 6. (**a**) Temperature-programmed reduction profiles (TPR) for all Ni/SiO_2 catalysts. TPR profiles of the BB(20) with 20 wt% Ni catalyst calcined at (**b**) 673 K and (**c**) 973 K with a Gaussian deconvolution of the signal. *Conditions:* $m_{cat} = 20\,mg$, $\beta = 10\,K\,min^{-1}$, $\dot{V}_{H_2/Ar} = 30\,mL_N\,min^{-1}$.

An increase in the calcination temperature to 973 K shifts the reduction profiles to higher temperatures. A small reduction peak is observed at 650 K, which is bulk NiO, but the main reduction occurs at 730 K. The main reduction peak is again caused by either 1:1 phyllosilicates or the migration of SiO_4. The peak with a temperature of 900 K at the maximum can be a result of 2:1 phyllosilicates ($Ni_3Si_4O_{10}(OH)_2$), which are even more stable than the 1:1 silicates and have a reduction peak ranging

from 873 to 1028 K [55]. When comparing the TPR profiles of the uncalcined samples with the ones calcined at 673 K, it can be seen that the main reduction peak increases slightly to higher temperatures for a loading of 20 wt%. At the same time, it decreases to lower temperatures for a metal loading of 10 wt%. In the one-step calcination and reduction process, it is possible to create even smaller and more dispersed Ni crystals compared to the classical calcination before reduction [62]. The shift to high temperatures can result from smaller NiO crystals, which are harder to reduce [54]. Since the smaller crystals provide a higher contact area to the silica surface, it is also possible that silicates are more easily formed, which increases the reduction temperature as well. The second explanation is more likely since the Ni particle size of the catalyst with BB(8), 10 wt% without calcination (2.0 nm) and with calcination (2.5 nm), does not differ significantly, whereas the peak temperature changes by 50 K. It seems that the presence of H_2 amplifies the formation of Ni silicates.

The particle size of the primary SiO_2 particles has only a small influence on the reduction profiles for the calcined samples. The TPR profiles reveal a higher share of hard to reduce species, e.g., the height of the main reduction peak is decreased compared to the BB(20) profile, and the height of the high-temperature peak is increased. The small particles provide a higher surface area and, therefore, facilitate the formation of Ni silicates, which form especially at the metal/support interface [55,60]. For the uncalcined catalysts, the difference is more pronounced and the main reduction peak is shifted to higher temperatures of 700 K.

Interesting TPR results are obtained for the alumina catalyst, which are displayed in Figure 7. The uncalcined samples also shows a nitrate decomposition peak. A broad low-intensity second peak is observed, starting at 700 K with the maximum at 1050 K. The peak is clearly the reduction of $NiAl_2O_4$, also evidenced by the XRD patterns and the shift of the γ-Al_2O_3 reflection (see Figure S4). Contributions at lower temperatures arise from Ni^{2+} ions incorporated into octahedral and tetrahedral voids in the alumina lattice [38,59]. After calcination at 673 K for 3 h, the first peak is removed and a broad low-temperature reduction peak is observed. The reduction sets in at 800 K and reaches the maximum at 1050 K again for the samples with 10 wt%. Calcination at 973 K shifts the starting point and the peak to even higher temperatures. Higher calcination temperatures favor the formation of the crystalline $NiAl_2O_4$, which is also observed by XRD (see Figure S4).

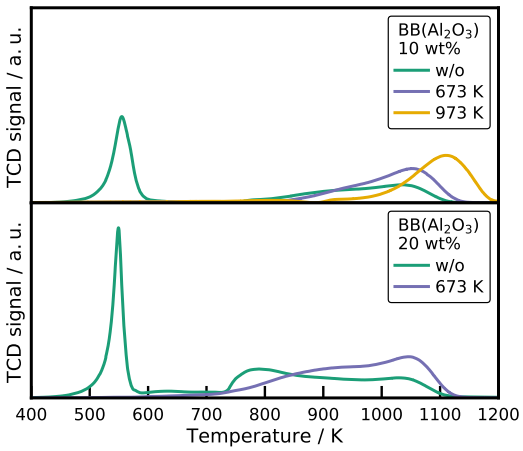

Figure 7. The TPR profiles of the spray-dried Ni/Al_2O_3 catalysts. *Conditions:* $m_{cat} = 20$ mg, $\beta = 10\,K\,min^{-1}$, $\dot{V}_{H_2/Ar} = 30\,mL_N\,min^{-1}$.

For the sample with a higher loading of 20 wt%, an additional peak at 800 K is observed corresponding to Ni^{2+} incorporated into octahedral voids in the alumina lattice [38]. The calcined samples show the same behavior as for the lower Ni loading. Surprising is that even for the uncalcined catalyst, the main reduction peak is in a temperature range for small NiO crystals and $NiAl_2O_4$. The XRD pattern shows only reflections for crystalline $NiAl_2O_4$ and no NiO reflections at all.

2.7. Temperature-Programmed Desorption

Figure 8a displays the recorded desorption profiles after CO_2 adsorption at flow conditions for the catalysts with BB(8),10 wt% and BB(20), 20 wt%. The CO_2 desorption from the Ni/γ-Al_2O_3 catalyst (20 wt% without calcination) is shown in Figure 8b. Nearly identical profiles were observed for all catalysts. CO_2 starts to desorb at a temperature of 380 K, reaches the maximum desorption rate around 450 K and shows a long tailing up to 800 K. At high temperatures, it is possible to observe the desorption of CO with a maximum at 700 K. The height of the desorption profiles decreases for the catalysts, which were calcined at higher temperatures and consequently have a smaller Ni surface area. No significant differences are observed between the CO_2 desorption from the Ni/SiO_2 catalysts and the Ni/γ-Al_2O_3 catalyst (see Figure 8b). In addition, no clear effect of the Na concentration on the CO_2 desorption profiles from the catalysts with 20 wt% calcined at 673 K with BB(20) and BB(8) is obtained.

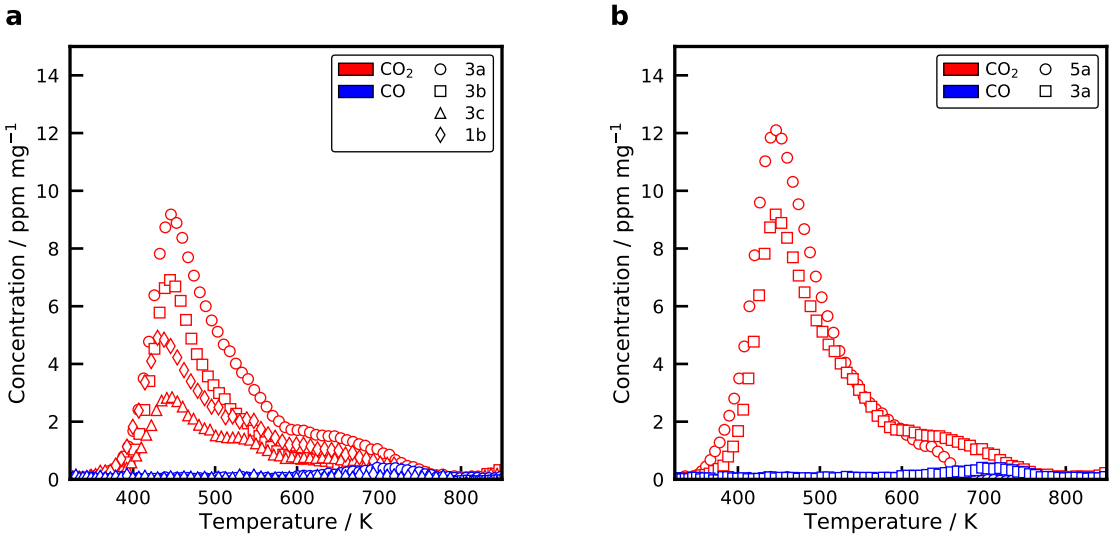

Figure 8. Temperature-programmed desorption of selected (**a**) Ni/SiO_2 catalysts and (**b**) Ni/γ-Al_2O_3 catalysts after CO_2 adsorption at flow conditions at 383 K for 1 h. *Conditions:* $m_{cat} = 30$ mg, $\beta = 20\,K\,min^{-1}$, $\dot{V}_{Ar} = 30\,mL_N\,min^{-1}$.

CO_2 uptakes for the Ni/SiO_2 catalysts, measured with volumetric adsorption and listed in Table 1 show a similar trend as the desorption profiles. Catalysts with a high Ni surface area adsorb more CO_2. It is also demonstrated that the formation of phyllosilicates, which are created at high calcination temperatures, does not form additional basic adsorption sites for CO_2. However, the Ni/Al_2O_3 catalyst adsorbs more CO_2 compared to the Ni/SiO_2 catalyst with the highest metal surface area. The Ni/γ-Al_2O_3 has a smaller metal surface area, but a high amount of basic adsorption sites on the γ-Al_2O_3 surface. CO_2 can form weak, medium or strong bonds with the basic adsorption sites [63]. Usually, it is assumed that CO_2 adsorbs only at basic sites on the support. However, Ewald and Hinrichsen [63] showed that CO_2 dissociates under flow conditions at an elevated temperature and adsorbs onto the Ni surface. It is, therefore, of great interest to deconvolve the desorption profiles in the desorption from basic sites and from the Ni surface. Due to the close resemblance of the desorption profiles from the silica and alumina catalysts, it indicates that the binding strength on the Ni surface and on basic sites is similar.

2.8. Activity of the Catalysts

Classical isothermal kinetic measurements are the most often used tool to screen the activity of catalytic materials. The drawback of this method is the time consumption to attain new steady-states. That is why only a few points in the conversion-temperature diagrams are typically mapped. The temperature-scanning technique developed by Wojciechowski and Asprey [32,33]

amplifies this process by applying a temperature ramp as during the temperature-programmed reduction. The concentration profile obtained with the temperature-scanning technique is displayed in Figure 9a for the catalyst 1b (BB(8), 10 wt%, calcined at 673 K) with a temperature ramp of 20 K min^{-1}. Concentration profiles are reported on a dry basis because of an inaccurate measurement of the H_2O concentration due to condensation in piping. The solid lines in Figure 9 are the equilibrium composition, which is calculated via the minimization of the free Gibbs energy using Cantera [64]. Thermodynamic properties of the gas-phase species were taken from the Active Thermochemical Tables (ATcT) [65,66]. Methane formation sets in at a temperature of approximately 500 K. It goes through a maximum at 650 K before it reaches the equilibrium concentration. CO forms directly at the beginning, together with CH_4, and goes through a local maximum at 580 K, which is illustrated in more detail in Figure 9b.

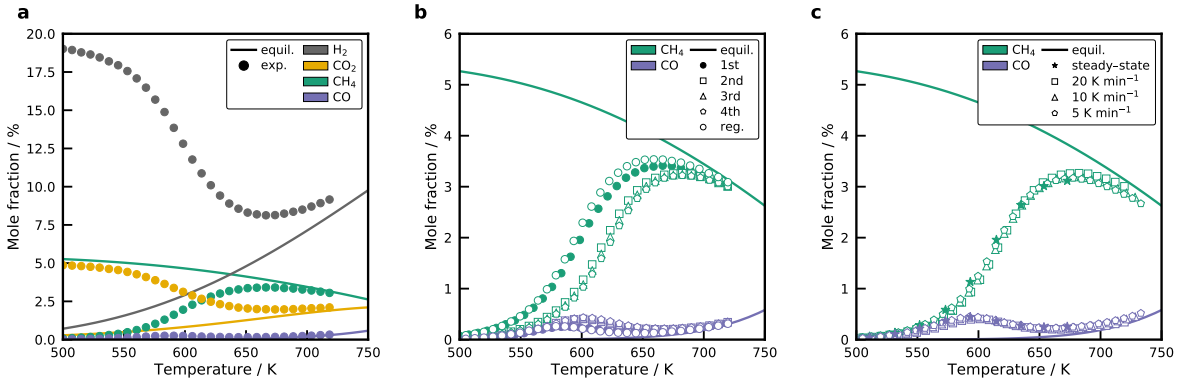

Figure 9. (**a**) Concentration profile (on a dry basis) of the temperature-scanning experiment for the catalyst formed using BB(8), 10 wt%, and calcined at 673 K (1b) compared to the equilibrium composition. (**b**) Repeated temperature-scanning results for the 1b catalyst with a temperature ramp of 20 K min^{-1}. After the fourth run, the sample was regenerated by oxidation in synthetic air at 773 K and reduced again. (**c**) Comparison of temperature-scanning profiles for different scanning rates, as well as steady-state results for the 1b sample. Experimental data is reduced for presentation. *Conditions:* $m_{cat} = 30$ mg, $WHSV = 100\,L_N\,h^{-1}\,g^{-1}$.

Consecutive scans were performed to investigate the reproducibility of the recorded profiles, which is illustrated in Figure 9b for the 1b sample. A significant deactivation is observed between the first and the second run. The CH_4, as well as the CO profile, are shifted by a value of 20 K to higher temperatures. Also, the CH_4 maximum decreases, whereas the local CO maximum increases slightly. All subsequent runs coincide with the profile of the second run. When the sample is regenerated by oxidation with synthetic air at 773 K for 60 min and reduced again, it is possible to restore the initial activity. The methane and CO profile can then be reproduced. This indicates a reversible blocking of sites with a high activity on the Ni surface, most probably surface carbon in the Ni steps [67] and excludes sintering of the Ni crystals as a possible reason. The Ni particles do not sinter easily after they have been reduced, which was also observed by Burattin et al. [55,60]. Carbon deposits decrease the available Ni surface area and, thereby, reduce the activity of the catalyst. During the oxidation, oxygen reacts with the carbon deposits to form CO_2 and the cleaned NiO surface remains with the initial NiO particle size. The applied temperature-scanning method does not allow to make predictions on the long-term stability, though.

The temperature-scanning method requires that the temperature ramp is low enough to reach a steady-state at each temperature increment. Results from the temperature-scanning experiment were, therefore, compared for different temperature ramps of 5 K min^{-1}, 10 K min^{-1}, and 20 K min^{-1} in Figure 9c. No significant differences were observed among the recorded profiles. Steady-state experiments also agree well with the transient experiment. This proves that it is possible to use the proposed technique for a fast screening of the prepared catalysts. The temperature-scanning

method allows the non-isothermal screening of catalysts in a temperature range of 500 to 800 K, which is important for CO_2 methanation. We want to highlight that this method has high potential for the screening of methanation catalysts, since the whole experiment takes only 30 min compared to several hours for the testing of only a few points on the conversion-temperature curve. For the CO_2 methanation mechanism on the Ni surface, this has to mean that new steady-states are obtained very fast.

Figure 10a displays the measured CO_2 conversion for the Ni/SiO_2 catalysts. The carbon mass balance is always closed within ±2%. Selectivity profiles show a low CH_4 selectivity at low temperatures. At the beginning of the methane formation at around 500 K, a more or less distinct formation of CO is observed. The CO concentration surpasses a maximum and declines with increasing temperature. Since this peak is also observed in the steady-state experiments, it can be ruled out as desorption from adsorbed CO, which could have been created during the dissociative adsorption of CO_2 at low temperatures. Weatherbee and Bartholomew [68] observed a CO formation on Ni/SiO_2 catalysts at low temperatures as well. It has to be kept in mind that the overall conversion is low, so it does not significantly affect the CH_4 yield. CO_2 dissociates on the Ni surface to form adsorbed CO^*. Due to the high binding energy of CO^*, the Ni surface is nearly entirely covered with CO^* at low temperatures, which blocks the adsorption of H_2. When the temperature is increased, CO^* will start to desorb, enabling the adsorption of H^* and the methane formation sets in. This can explain the local maximum of CO at the beginning of the methane formation. The influence of calcination temperature on the performance of the catalysts is similar for all BB and Ni loadings. An increase in the calcination temperature leads to a decrease in the activity of the catalyst. Conversion profiles are shifted to higher temperatures and the highest possible conversion is obtained for the samples without further thermal pretreatment. Next to the decrease in the CO_2 conversion, the selectivity to methane decreases as well. This includes the selectivity at low temperatures, as well as at the conversion maximum. On the one hand, the higher calcination temperatures produce larger Ni nanoparticles, which will have a lower Ni surface area and a higher share of Ni terrace sites. On the other hand, the particles have a stronger metal/support interaction.

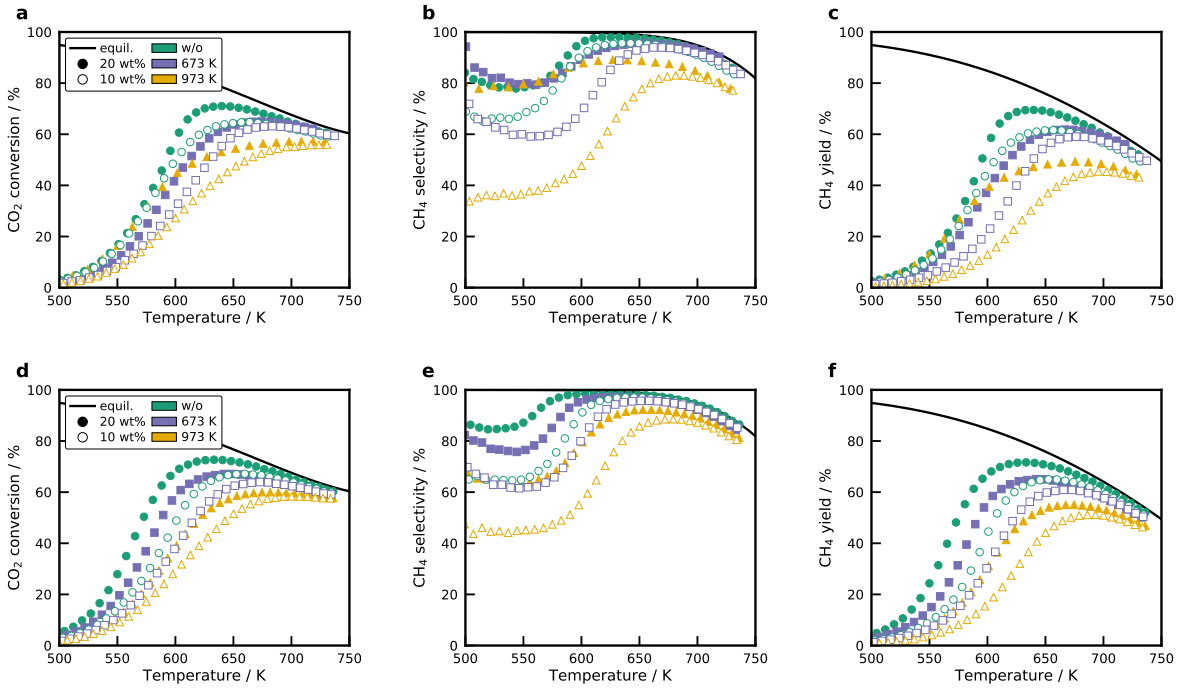

Figure 10. CO_2 conversion, CH_4 selectivity, and CH_4 yield for BB(20) (**a**–**c**) and BB(8) (**d**–**f**). Solid lines represent the equilibrium. All figures share the same legend. *Conditions:* $m_{cat} = 30\,mg$, $\beta = 20\,K\,min^{-1}$, $WHSV = 100\,L_N\,h^{-1}\,g^{-1}$.

The usage of different sizes of the SiO_2 primary particles affects the size of the Ni crystals, as shown in the characterization section. Comparing the conversion profiles at loadings of 10 wt% and 20 wt% shows that the smaller primary particle size is also beneficial in terms of activity and CH_4 selectivity. Obviously, an increase in metal loading leads to a higher CO_2 conversion. However, the true activity changes cannot be determined by comparing the conversion. Instead, the turnover frequency needs to be compared. Interesting results are obtained for the selectivity profiles. A higher selectivity towards methane is obtained for the catalysts with a higher metal loading. The highest methanation activity is obtained for the catalysts with BB(8), 20 wt% Ni, and without thermal treatment, which has the highest metal surface area. Those samples with a small Ni loading of 10 % and high calcination temperature of 973 K have the lowest methane yield. The proposed spray-drying method shows a high potential for producing optimized Ni/SiO_2 catalysts with higher metal surface areas by increasing the Ni loading further without adjusting the physical properties, such as the pore size.

Figure 11 shows the results for the temperature-scanning of the $Ni/\gamma\text{-}Al_2O_3$ catalysts. Only two catalysts were tested, which have a Ni loading of 20 wt%. These catalyst exhibit a reasonable H_2 uptake despite the low *DOR*, indicating finely dispersed NiO particles. Surprisingly, the $Ni/\gamma\text{-}Al_2O_3$ catalyst without calcination reaches a maximum CO_2 conversion of 71 %, which is close to the performance of the best Ni/SiO_2 catalyst (BB(8), 20 wt%, without calcination) with 73 %. In addition, the CH_4 selectivity is superior to the Ni/SiO_2 catalyst. For the catalyst that was calcined at 673 K it can be observed that the activity drops, which is expected due to the lower *DOR*. The decrease in activity is accompanied by a lower CH_4 selectivity. As shown in by the TPD results and the CO_2 chemisorption, the $\gamma\text{-}Al_2O_3$ support provides a high share of basic adsorption sites that interact strongly with CO_2. Moreover, basic sites play an important role in the CO_2 methanation mechanism, and can improve the activity by altering the mechanism [15].

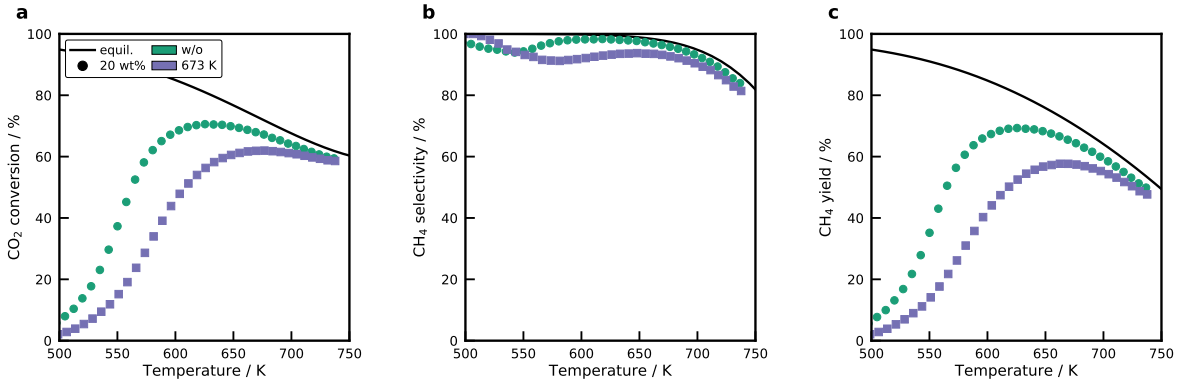

Figure 11. (**a**) CO_2 conversion, (**b**) CH_4 selectivity, and (**c**) CH_4 yield for the $Ni/\gamma\text{-}Al_2O_3$ catalysts. Only the two catalysts were tested, which have a sufficient *DOR*. *Conditions:* $m_{cat} = 30\,mg$, $\beta = 20\,K\,min^{-1}$, $WHSV = 100\,L_N\,h^{-1}\,g^{-1}$.

Ni aluminates can also be used industrially for high-temperature processes, where the required high reduction temperatures can be attained such as the dry reforming of CH_4 [69]. The strong interaction of Ni aluminates or Ni silicates serves as anchoring site for the Ni crystals once they are reduced. These anchoring sites can prevent sintering of the Ni and provide small Ni crystals at high temperatures and, consequently, a high active surface area [69].

2.9. Activation Energies and Turnover Frequencies

Reaction rates for the CH_4 formation were calculated based on the differential fixed-bed assumption, which allows an evaluation up to a conversion of 10 %. Figure S9 shows the Arrhenius dependence of the methane formation rates for selected catalysts. The slope does not change much between the different catalysts and an average activation energy of $84 \pm 4\,kJ\,mol^{-1}$ is obtained for all Ni/SiO_2 catalysts. The values agree well with the literature data, which is in the range

of 75 to 88 kJ mol^{-1} [16,68,70–72]. The Ni/Al_2O_3 catalyst has an activation energy of 76 kJ mol^{-1}, which reasonable compares to literature data [23,38]. Figure 12a shows the turnover frequencies, calculated for the Ni/SiO_2 catalysts at a constant temperature of 530 K.

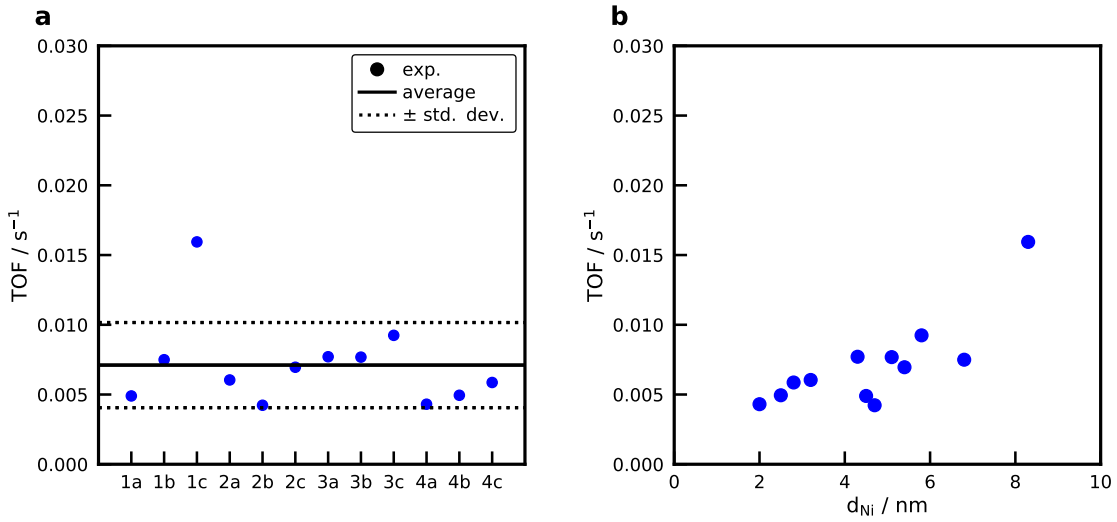

Figure 12. (**a**) Turnover frequencies (CO_2 to CH_4) of the Ni/SiO_2 catalysts at a temperature of 530 K. For the naming convention of the samples refer to the production tree Figure 1. (**b**) Turnover frequency in dependence of the Ni particle size. *Conditions:* $m_{cat} = 30$ mg, $\beta = 20$ K min^{-1}, $WHSV = 100\,L_N\,h^{-1}\,g^{-1}$, $X_{CO_2} < 10$ %.

At this temperature, the CO_2 conversion for all catalysts is below 10 %. This means that the concentration in the gas phase varies, but the difference is small that is why it can be neglected. An average TOF of $7.1 \cdot 10^{-3}\,s^{-1}$ is obtained for all samples. The Ni/γ-Al_2O_3 show a significantly higher TOF of $37.1 \cdot 10^{-3}\,s^{-1}$. Figure 12b shows the TOF as a function of the Ni crystal size determined with XRD, revealing no correlation between the Ni crystal size and the TOF. The catalyst 1c (BB(20), 20 wt%, calcined at 973 K) with a Ni crystal size of 8.3 nm shows a significantly higher activity compared to the rest of the catalysts. This is in contrast to results from Vogt et al. [73] who report a clear structure-sensitivity for the CO_2 methanation below 6 nm with a maximum TOF at approximately 2 nm, at a temperature of 673 K for Ni/SiO_2 catalysts. On the other hand, no structure sensitivity is observed by Beierlein et al. [38] for the CO_2 methanation on Ni/Al_2O_3 catalysts. Usually, the equilibrium shape of the Ni crystal changes significantly below 7 nm and reaches a nearly constant facet distribution for bigger crystals [74], which explains why a structure-sensitivity should be observed in small Ni crystals. However, Weber et al. [75] observed a maximum TOF for the CO methanation at 15 nm on gasborne Ni nanoparticles. Due to the fast evaporation of the water in the droplets in the spray-drying procedure and the high cooling rates, it is questionable whether the equilibrium shape of the Ni crystal is obtained. As a conclusion, we can say that for the studied operation point at 530 K and conversion below 10 % no clear structure-activity relation can be derived for the spray-dried Ni/SiO_2 catalysts. More catalysts with larger Ni crystal sizes need to be produced to provide a clearer trend that can now be easily done by applying the tailoring guide in Figure 5c.

3. Materials and Methods

3.1. Materials

Ammonium stabilized aqueous colloidal silica suspensions with an average particle diameter of 8 nm (Köstrosol 0830AS, 30 wt%, pH 9.6), 20 nm (Köstrosol 2040AS, 40 wt%, pH 9.3), and 45 nm (Köstrosol 0830AS, 30 wt%, pH 9.6) were obtained from CWK Chemiewerk Bad Köstritz GmbH (Bad Köstritz, Germany). The silica nanoparticles were used as support for the NiO nanoparticles.

Colloidal Al_2O_3 nanoparticle suspension (pseudo-Boehmite, (AlO(OH)) 50 nm, 20 wt%, pH 4, Alfa Aesar, Ward Hill, MA, USA) was also used as a support for the NiO nanoparticles. Nickel nitrate, $Ni(NO_3)_2 \cdot 6\,H_2O$ (99 %, Sigma-Aldrich, St. Louis, MO, USA), was added to the suspension as the precursor for the production of nickel oxide nanoparticles. Deionized water was utilized in all synthesis suspensions. All of the materials in this work were used without further purification.

3.2. Experimental Setup and Synthesis of the NiO/SiO_2 Nanoparticles

The particles synthesized in this study were produced by spray-drying a colloidal silica suspension containing dissolved $Ni(NO_3)_2$ and deionized water. Prepared suspensions (pH of approximately 6.7) were atomized using an aerosol nebulizer (AGK 2000, Palas GmbH, Karlsruhe, Germany), with pressurized air as carrier gas at a flow rate of 7.7 L min^{-1}. The produced droplets were dried in a tube furnace at 673 K with a short residence time of 1.6 s. The dried particles, also named as BB, were collected on a filter and heat-treated in a muffle oven to adjust the NiO nanoparticle size. A schematic drawing of the setup can be found in previous work [31]. In this study, NiO nanoparticles supported on two different supports (SiO_2 and Al_2O_3) with two different Ni loadings (10 and 20 wt%) for two different heat treatment conditions were investigated. For the NiO nanoparticles supported on silica, BB formed with two different SiO_2 primary particle sizes (8 and 20 nm) were produced and characterized. For the NiO nanoparticles supported on alumina, BB created with Al_2O_3 primary particles with a size of 50 nm were synthesized as well. Figure 1 summarizes the catalysts produced within this work.

3.3. Physical Characterization

The structure and morphology of the catalysts were examined with transmission electron microscopy (TEM) and scanning electron microscopy (SEM). TEM was performed with a JEOL JEM-2100 microscope (JEOL Ltd., Akishima, Tokyo, Japan) operated at 160 kV. For the preparation of the TEM samples, the particles were deposited onto a copper grid coated with a carbon film. SEM was carried out with a Zeiss DSM Gemini 982 (Zeiss, Jena, Germany) operated at 5 kV.

X-ray diffraction (XRD) diagrams were recorded in $\omega/2\Theta$-geometry using Cu-Kα radiation ($\lambda = 1.5406$ Å) operated at 40 kV and 40 mA (Empyrean, PANalytical, Almelo, Netherlands). Angles of 2Θ between 10 and 90° were measured with a step length of 0.026° and a step time of 200 s. The NiO nanoparticle size was determined using the Scherrer equation (1) with a shape factor $k = 0.9$ and the line broadening of the NiO(200) line at $2\Theta = 43.3°$. The full width at half-maximum of the reflection was corrected using LaB_6 as a reference.

$$d = \frac{K_f \lambda}{\beta cos(\Theta)} \quad (1)$$

Small-angle X-ray scattering (SAXS) was used to measure the size of the single primary particles that form the BB. These experiments took place on the above-described diffractometer equipped with a SAXS stage operated at 45 kV and 40 mA. The produced particles were placed in a sample holder between two mylar foils and were measured in a range from −0.115 to 5° 2Θ, with a step size of 0.01° 2Θ for 2.2 s per step. Nitrogen adsorption–desorption isotherms were recorded at 77 K (ASAP 2020, Micromeritics Instrument Corporation, Norcross, GA, USA). The Brunauer-Emmett-Teller (BET) method was used to calculate the specific surface area of the BB. The pore size distributions and total pore volume of the BB were calculated according to the Barrett-Joyner-Halenda (BJH) model, using the results from the desorption. Typically, a sample mass of 100 to 150 mg was degassed at a temperature of 250 °C for 2 h before analysis.

3.4. Chemical Characterization

Temperature-programmed reduction (TPR) experiments were conducted in the BelCat-M device (MicrotracBEL Corp., Osaka, Japan). 20 mg of the catalyst were degassed at 393 K for 60 min in Ar atmosphere to remove adsorbed species. The TPR was conducted with a 10 % H_2/Ar mixture at a volumetric flow rate of 30 $mL_N\,min^{-1}$ and the temperature was linearly raised with a temperature ramp of 10 $K\,min^{-1}$ from 323 to 1223 K. A thermal conductivity detector (TCD) was used to analyze the hydrogen consumption after the effluent gas was passed over a molecular sieve with a pore size of 3 Å. The amount of Ni in the sample was determined by assuming that only NiO was reduced and the TCD was calibrated for a NiO reference (99.998 %, AlfaAesar, Ward Hill, MA, USA).

The nickel dispersion and crystallite size were measured by H_2 adsorption and subsequent O_2 titration in a volumetric adsorption apparatus (3Flex, Micromeritics Instrument Corporation, Norcross, GA, USA). A sample of 80 mg was reduced at 723 K for 1 h in pure H_2 with a volumetric flow rate of 50 $mL_N\,min^{-1}$. All gases used in this study were of quality 5.0 and passed over O_2 and H_2O traps to remove contaminants. After reduction, the catalyst was evacuated for 1 h before the sample was cooled to the adsorption temperature of 323 K. An adsorption isotherm was recorded from 3 to 550 mbar with an equilibration interval of 1 min. Following the H_2 adsorption, the sample was heated in vacuum to 673 K (10 $K\,min^{-1}$) and evacuated for 1 h before the O_2 adsorption was carried out at this temperature. Back-extrapolation of the linear part of the isotherm to zero pressure was used to calculate the uptake of either H_2 or O_2. From the adsorption experiments, the degree of reduction (*DOR*) (Equation (2)), the corrected dispersion *D* (Equation (5)), the specific metal surface area a_{Ni} (Equation (3)), and the Ni crystallite size d_{Ni} (Equation (4)) were calculated. CO_2 adsorption isotherms are also recorded for selected samples. Due to a strong adsorption of CO_2 on possible basic surface sites, a double isotherm was performed.

$$DOR = \frac{a_{cat} f_{calibration}}{2 m_{cat} Q_{O_2}} \tag{2}$$

$$a_{Ni} = Q_{H_2} z N_A \sigma_{Ni} \frac{1}{DOR} \tag{3}$$

$$d_{Ni} = \frac{6000 \omega_{Ni}}{\rho_{Ni} a_{Ni}} \tag{4}$$

$$D = 2 a_{Ni} W_{Ni} \frac{100}{\omega_{Ni}} \tag{5}$$

A spherical shape of the Ni crystals was assumed [76] and the following parameters were used: M_{NiO} is the molar mass (58.69 $g\,mol^{-1}$), N_A is the Avogadro constant, ω_{Ni} the Ni loading, σ_{Ni} is the surface area of a Ni atom (6.51 $Å^2$), and ρ_{Ni} is the Ni density (8.9 $g\,cm^{-3}$).

CO_2 temperature-programmed desorption was applied to investigate the interaction of CO_2 with basic sites on the support and the Ni crystals. A mixture of 9.87% CO_2 in He is passed over the catalyst in a flow experiment at 383 K for 60 min. Then the catalyst is purged with Ar for 15 min and cooled to 323 K to start the TPD with a temperature ramp of 20 $K\,min^{-1}$ to 1073 K.

3.5. Methanation Experiments

CO_2 methanation experiments were conducted in the BelCat-M connected to a mass spectrometer (MS) (GAM200, InProcessInstruments, Bremen, Germany). 30 mg of the sample was placed in a modified sample holder [53] and fixed with quartz wool plugs. A temperature-scanning experiment was performed to investigate the activity of the catalysts. In these experiments, a stoichiometric mixture of H_2/CO_2 with Ar as internal standard (20/5/75 %) flowed through the catalyst bed with a volumetric flow rate of 50 $mL_N\,min^{-1}$, and the temperature was raised with a constant heating rate of 20 $K\,min^{-1}$ from 323 K to 723 K. A thermocouple was placed directly above the catalyst bed. The exit gas concentration was measured with the MS, which was calibrated with certified gas mixtures for

H_2, CO_2, CO, CH_4 and Ar. A measurement time of 0.4 s per cycle was achieved. The CO_2 conversion (X_{CO_2}), CH_4 selectivity (S_{CH_4}), and CH_4 yield (Y_{CH_4}) were determined from the measured exit gas composition with Equations (6) to (8) using Ar as an internal standard.

$$X_{CO_2} = 1 - \frac{x_{Ar}^{in} x_{CO_2}^{out}}{x_{Ar}^{out} x_{CO_2}^{in}} \tag{6}$$

$$S_{CH_4} = \frac{x_{CH_4}^{out}}{x_{CH_4}^{out} + x_{CO}^{out}} \tag{7}$$

$$Y_{CH_4} = S_{CH_4} X_{CO_2} \tag{8}$$

Reaction rates were calculated at temperatures where the conversion was below 10 %, so that differential fixed-bed conditions could be assumed. The methane formation rate r_{CH_4} was calculated with

$$r_{CH_4} = \frac{\dot{V}_N^{in} \alpha x_{CH_4}^{out} p_N}{m_{cat} R T_N} \tag{9}$$

where α accounts for the volume contraction with the change in the concentration of the internal standard Ar. The activation energy was determined from the calculated rates and temperatures. In combination with the amount of exposed Ni atoms measured with H_2 adsorption, it was possible to determine the turnover frequency *TOF*:

$$TOF = \frac{r_{CH_4}}{2 Q_{H_2}} \tag{10}$$

4. Conclusions

Highly dispersed NiO nanoparticles supported on silica with a well organized porous structure and tunable properties were produced by spray-drying. According to our experimental results, we proved that the presented method is a flexible process that can be extended for the preparation of the catalyst particles containing different metals, which was done in previous work for Co_3O_4/SiO_2 catalysts. With this method, the pore size, the total pore volume, and the specific surface area of the catalyst can be easily adjusted by varying the primary particle size of the SiO_2 support. One of the biggest advantages of the method presented here for the NiO/SiO_2 system is the independent control of the NiO nanoparticle size and the pore size. The size of the NiO nanoparticles can be tailored with the ratio of the mass of Ni to the surface area of the support and calcination temperature, whereas the pore size depends only on the size of the primary SiO_2 particle.

Ni/SiO_2 catalysts with metal surface areas of up to $40\,m^2\,g^{-1}$ and 42 % dispersion were synthesized. These catalysts were produced without further thermal treatment and the decomposition of remaining nitrates occurred during the reduction. In order to increase the metal surface area, it is, therefore, of interest to produce the particles in H_2 atmosphere. $Ni/\gamma\text{-}Al_2O_3$ catalysts were produced with the same method, but it is not possible to tailor the catalyst properties as good as for the Ni/SiO_2 catalysts. The finely dispersed NiO in close contact with a high surface area alumina leads to the formation of crystalline $NiAl_2O_4$, which is challenging to reduce but can provide a well-dispersed catalyst for high-temperature processes. The spray-drying procedure is a universal method that can be extended to various catalytic systems and even used to produce bimetallic catalysts.

The temperature-scanning methanation experiment allowed for a fast and efficient screening of the catalysts. The catalyst with the highest metal surface area showed the highest methane yield. Selectivity toward CO depends on the metal/support interaction. High calcination temperatures lead to the formation of Ni phyllosilicates, which are difficult to reduce. The highest activity and Ni surface area were observed for those samples without further thermal treatment. Since the crystal size was varied for the catalysts, it was possible to investigate the structure-activity relations for the

CO_2 methanation for the Ni/SiO_2 and Ni/γ-Al_2O_3 catalysts. The Ni/γ-Al_2O_3 catalyst showed a high methanation activity due to the presence of basic sites on the support. No conclusive dependence of the TOF on the Ni crystal size was observed for the Ni/SiO_2 catalysts. The tailoring guide proposed in this work will now allow to design Ni/SiO_2 catalysts with defined Ni crystal sizes that will be investigated with the temperature scanning technique in a Berty reactor setup to unravel structure-activity relations for higher temperatures and conversions.

Supplementary Materials: The following are available online at http://www.mdpi.com/2073-4344/10/12/1410/s1, Figure S1: (a) BET surface area and pore volume of SiO_2 with BB(20) at different calcination temperatures. (b) SEM image for the calcination at 673 K. (c) SEM image after calcination at 1273 K. Figure S2: (a) BET surface area and pore volume of the Al_2O_3 at different calcination temperatures. (b) Pore size distribution for different calcination temperatures. Figure S3: TEM micrograph of Ni/SiO_2 catalyst with (a) BB(8) with 20 wt% calcined at 673 K and (b) BB(45) with 5 wt calcined at 673 K. Table S1: Mass loss due to the decomposition of remaining nitrates during the reduction of the catalysts without additional heat treatment. Figure S4: (a) XRD patterns of the spray-dried Ni/Al_2O_3 catalyst after production and after calcination at 673 K. (b) XRD patterns of BB(Al_2O_3) calcined at 673 K with different nickel loadings. (c) Lattice constant of the crystalline structure as a function of the Ni loading in BB(Al_2O_3). Table S2: Average NiO particle sizes determined with XRD for the Ni/SiO_2 catalysts with different Ni loadings and SiO primary particle sizes after calcination at different temperatures. , Figure S5: (a) XRD patterns for the BB(20) catalyst with 20 wt% calcined at 673 K. (b) XRD pattern for the same catalyst after reduction and passivation. Figure S6: SAXS measurement of BB(20) with 20 wt% calcined at 673 K, Figure S7: (a) Volumetric adsorption isotherms for H_2 adsorption on BB(8), 20 wt% at different calcination temperatures. (b) CO_2 adsorption isotherm for the Ni/SiO_2 catalyst with BB(8), 20 wt%, without calcination and the pure SiO_2 support. Figure S8: TPR profile of the Ni/SiO_2 (BB(8), 10 wt%, without calcination) recorded with the MS. Figure S9: Arrhenius diagram for selected Ni/SiO_2 catalysts.

Author Contributions: Conceptualization, B.K., A.M.A, A.P.W., and T.T.; formal analysis, B.K., A.M.A.; investigation, B.K., A.M.A.; writing—original draft preparation, B.K., A.M.A., J.M.; writing—review and editing, J.M., A.P.W., T.T.; visualization, B.K., A.M.A.; supervision, T.T., A.P.W.; funding acquisition, T.T., A.P.W. All authors have read and agreed to the published version of the manuscript.

Funding: The authors gratefully acknowledge financial support from the Deutsche Forschungsgemeinschaft (DFG, German Research Foundation) within the SPP 1570 with the project number WE 2331/13-3 and TU 89/9-3 and the DFG project 290019031. Part of this work is supported and financed by Clausthal University of Technology, project Catalytic and Microbial Methanation as Basis for Sustainable Energy Storage (CliMb).

Acknowledgments: The authors thank the Institute of Mineral and Waste Processing, Waste Disposal and Geomechanics of Clausthal University of Technology (ICP-OES) and CWK Chemiewerk Bad Köstritz GmbH for providing colloidal silica nanoparticles. A.M. and B.K. gratefully acknowledge the fruitful discussions on the XRD with Alessio Zandona. We acknowledge financial support by the Open Access Publishing Fund of Clausthal University of Technology.

Conflicts of Interest: The authors declare no conflict of interest.

Abbreviations

The following abbreviations are used in this manuscript:

TPR	Temperature-programmed reduction
TPD	Temperature-programmed desorption
XRD	X-ray diffraction
TEM	Transmission Electron Microscopy
SEM	Scanning Electron Microscopy
TCD	Thermal conductivity detector
MS	Mass spectrometer
BB	Building-Blocks
SAXS	Small-angle X-ray scattering
BET	Brunauer-Emmett-Teller method
BJH	Barrett-Joyner-Halenda model

List of Symbols

Latin symbols		
a	area	m^2
D	dispersion	-
DOR	degree of reduction	%
d	diameter	m
f	calibration factor	$mol\,m^{-2}$
K	Scherrer form factor	-
m	mass	g
p	pressure	bar
Q	adsorbed amount	$mol\,g^{-1}$
R	ideal gas constant	$J\,mol^{-1}\,K^{-1}$
r	reaction rate	$mol\,s^{-1}\,g^{-1}$
S	selectivity	-
T	temperature	K
$\dot{V}$	volume flow	$mL\,min^{-1}$
W	molar mass	$g\,mol^{-1}$
w	metal loading	-
$WHSV$	weight hourly space velocity	$L_N\,h^{-1}\,g^{-1}$
X	conversion	-
x	molar fraction	-
Y	yield	-
z	adsorption stoichiometry	-

Greek symbols		
α	volume reduction $(x_{Ar}^{in}/x_{Ar}^{out})$	-
β	temperature ramp	$K\,min^{-1}$
Θ	Bragg angle	°
λ	wavelength	m
ρ	density	$kg\,m^{-3}$
σ	surface area	m^2

Subscripts	
calibration	calibration
cat	catalyst
f	form factor
N	normal conditions

Superscripts	
in	inlet
out	outlet

References

1. Tomiyama, S.; Takahashi, R.; Sato, S.; Toshiaki, S.; Satoshi, Y. Preparation of Ni/SiO_2 catalyst with high thermal stability for CO_2-reforming of CH_4. *Appl. Catal. A Gen.* **2003**, *241*, 349–361. [CrossRef]
2. Zhang, Y.; Wang, W.; Wang, Z.; Zhou, X.; Wang, Z.; Liu, C.J. Steam reforming of methane over Ni/SiO_2 catalyst with enhanced coke resistance at low steam to methane ratio. *Catal. Today* **2015**, *256*, 130–136. [CrossRef]
3. Huang, X.; Reimert, R. Kinetics of steam reforming of ethane on Ni/YSZ (yttria-stabilised zirconia) catalyst. *Fuel* **2013**, *106*, 380–387. [CrossRef]
4. Xie, Z.; Yan, B.; Lee, J.H.; Wu, Q.; Li, X.; Zhao, B.; Su, D.; Zhang, L.; Chen, J.G. Effects of oxide supports on the CO_2 reforming of ethane over Pt-Ni bimetallic catalysts. *Appl. Catal. B Environ.* **2019**, *245*, 376–388. [CrossRef]

5. Sehested, J.; Dahl, S.; Jacobsen, J.; Rostrup-Nielsen, J.R. Methanation of CO over nickel: Mechanism and kinetics at high H_2/CO ratios. *J. Phys. Chem. B* **2005**, *109*, 2432–2438. [CrossRef]
6. Nematollahi, B.; Rezaei, M.; Lay, E.N. Preparation of highly active and stable NiO-CeO_2 nanocatalysts for CO selective methanation. *Int. J. Hydrogen Energy* **2015**, *40*, 8539–8547. [CrossRef]
7. Rönsch, S.; Schneider, J.; Matthischke, S.; Schlüter, M.; Götz, M.; Lefebvre, J.; Prabhakaran, P.; Bajohr, S. Review on methanation—From fundamentals to current projects. *Fuel* **2016**, *166*, 276–296. [CrossRef]
8. Gao, J.; Liu, Q.; Gu, F.; Liu, B.; Zhong, Z.; Su, F. Recent advances in methanation catalysts for the production of synthetic natural gas. *RSC Adv.* **2015**, *5*, 22759–22776. [CrossRef]
9. Kreitz, B.; Wehinger, G.D.; Turek, T. Dynamic simulation of the CO_2 methanation in a micro-structured fixed-bed reactor. *Chem. Eng. Sci.* **2019**, *195*, 541–552. [CrossRef]
10. Kreitz, B.; Friedland, J.; Güttel, R.; Wehinger, G.D.; Turek, T. Dynamic Methanation of CO_2—Effect of Concentration Forcing. *Chem. Ing. Tech.* **2019**, *91*, 576–582. [CrossRef]
11. Kreitz, B.; Brauns, J.; Wehinger, G.D.; Turek, T. Modeling the Dynamic Power–to–Gas Process: Coupling Electrolysis with CO_2 Methanation. *Chem. Ing. Tech.* **2020**, *43*, 20332. [CrossRef]
12. Frontera, P.; Macario, A.; Ferraro, M.; Antonucci, P. Supported Catalysts for CO_2 Methanation: A Review. *Catalysts* **2017**, *7*, 59. [CrossRef]
13. Ashok, J.; Pati, S.; Hongmanorom, P.; Tianxi, Z.; Junmei, C.; Kawi, S. A review of recent catalyst advances in CO_2 methanation processes. *Catal. Today* **2020**. [CrossRef]
14. Wei, W.; Jinlong, G. Methanation of carbon dioxide: An overview. *Front. Chem. Sci. Eng.* **2011**, *5*, 2–10. [CrossRef]
15. Pan, Q.; Peng, J.; Sun, T.; Wang, S.; Wang, S. Insight into the reaction route of CO_2 methanation: Promotion effect of medium basic sites. *Catal. Commun.* **2014**, *45*, 74–78. [CrossRef]
16. Aziz, M.; Jalil, A.A.; Triwahyono, S.; Mukti, R.R.; Taufiq-Yap, Y.H.; Sazegar, M.R. Highly active Ni-promoted mesostructured silica nanoparticles for CO_2 methanation. *Appl. Catal. B Environ.* **2014**, *147*, 359–368. [CrossRef]
17. Chen, C.S.; Budi, C.S.; Wu, H.C.; Saikia, D.; Kao, H.M. Size-Tunable Ni Nanoparticles Supported on Surface-Modified, Cage-Type Mesoporous Silica as Highly Active Catalysts for CO_2 Hydrogenation. *ACS Catal.* **2017**, *7*, 8367–8381. [CrossRef]
18. Ye, R.P.; Gong, W.; Sun, Z.; Sheng, Q.; Shi, X.; Wang, T.; Yao, Y.; Razink, J.J.; Lin, L.; Zhou, Z.; et al. Enhanced stability of Ni/SiO_2 catalyst for CO_2 methanation: Derived from nickel phyllosilicate with strong metal-support interactions. *Energy* **2019**, *188*, 116059. [CrossRef]
19. Zhu, P.; Chen, Q.; Yoneyama, Y.; Tsubaki, N. Nanoparticle modified Ni-based bimodal pore catalysts for enhanced CO_2 methanation. *RSC Adv.* **2014**, *4*, 64617–64624. [CrossRef]
20. Huang, Y.J.; Schwarz, J.A. The effect of catalyst preparation on catalytic activity: I. The catalytic activity of Ni/Al_2O_3 catalysts prepared by wet impregnation. *Appl. Catal.* **1987**, *30*, 239–253. [CrossRef]
21. Li, G.; Hu, L.; Hill, J.M. Comparison of reducibility and stability of alumina-supported Ni catalysts prepared by impregnation and co-precipitation. *Appl. Catal. A Gen.* **2006**, *301*, 16–24. [CrossRef]
22. Ashok, J.; Ang, M.L.; Kawi, S. Enhanced activity of CO_2 methanation over Ni/CeO_2-ZrO_2 catalysts: Influence of preparation methods. *Catal. Today* **2017**, *281*, 304–311. [CrossRef]
23. Koschany, F.; Schlereth, D.; Hinrichsen, O. On the kinetics of the methanation of carbon dioxide on coprecipitated NiAl(O)$_x$. *Appl. Catal. B Environ.* **2016**, *181*, 504–516. [CrossRef]
24. Chiarello, G.; Rossetti, I.; Forni, L. Flame-spray pyrolysis preparation of perovskites for methane catalytic combustion. *J. Catal.* **2005**, *236*, 251–261. [CrossRef]
25. Compagnoni, M.; Tripodi, A.; Di Michele, A.; Sassi, P.; Signoretto, M.; Rossetti, I. Low temperature ethanol steam reforming for process intensification: New Ni/MxO-ZrO_2 active and stable catalysts prepared by flame spray pyrolysis. *Int. J. Hydrogen Energy* **2017**, *42*, 28193–28213. [CrossRef]
26. Saib, A.M.; Claeys, M.; van Steen, E. Silica supported cobalt Fischer–Tropsch catalysts: Effect of pore diameter of support. *Catal. Today* **2002**, *71*, 395–402. [CrossRef]
27. Borg, Ø.; Eri, S.; Blekkan, E.A.; Storsæter, S.; Wigum, H.; Rytter, E.; Holmen, A. Fischer–Tropsch synthesis over γ-alumina-supported cobalt catalysts: Effect of support variables. *J. Catal.* **2007**, *248*, 89–100. [CrossRef]
28. Song, D.; Li, J. Effect of catalyst pore size on the catalytic performance of silica supported cobalt Fischer–Tropsch catalysts. *J. Mol. Catal. A Chem.* **2006**, *247*, 206–212. [CrossRef]

29. Koirala, R.; Pratsinis, S.E.; Baiker, A. Synthesis of catalytic materials in flames: Opportunities and challenges. *Chem. Soc. Rev.* **2016**, *45*, 3053–3068. [CrossRef]
30. Gradon, L.; Balgis, R.; Hirano, T.; Rahmatika, A.M.; Ogi, T.; Okuyama, K. Advanced aerosol technologies towards structure and morphologically controlled next-generation catalytic materials. *J. Aerosol Sci.* **2020**, *149*, 105608. [CrossRef]
31. Martínez Arias, A.; Weber, A.P. Aerosol synthesis of porous SiO_2-cobalt-catalyst with tailored pores and tunable metal particle size for Fischer-Tropsch synthesis (FTS). *J. Aerosol Sci.* **2019**, *131*, 1–12. [CrossRef]
32. Wojciechowski, B. The temperature scanning reactor I: Reactor types and modes of operation. *Catal. Today* **1997**, *36*, 167–190. [CrossRef]
33. Asprey, S. The temperature scanning reactor III: Experimental procedures and data processing. *Catal. Today* **1997**, *36*, 209–226. [CrossRef]
34. Wojciechowski, B.; Asprey, S.P. Kinetic studies using temperature-scanning: The oxidation of carbon monoxide. *Appl. Catal. A Gen.* **2000**, *190*, 1–24. [CrossRef]
35. Liebner, C.; Wolf, D.; Baerns, M.; Kolkowski, M.; Keil, F.J. A high-speed method for obtaining kinetic data for exothermic or endothermic catalytic reactions under non-isothermal conditions illustrated for the ammonia synthesis. *Appl. Catal. A Gen.* **2003**, *240*, 95–110. [CrossRef]
36. Vogt, C.; Wijten, J.; Madeira, C.L.; Kerkenaar, O.; Xu, K.; Holzinger, R.; Monai, M.; Weckhuysen, B.M. Alkali Promotion in the Formation of CH_4 from CO_2 and Renewably Produced H_2 over Supported Ni Catalysts. *ChemCatChem* **2020**, *12*, 2792–2800. [CrossRef]
37. Le, T.A.; Kim, T.W.; Lee, S.H.; Park, E.D. Effects of Na content in $Na/Ni/SiO_2$ and $Na/Ni/CeO_2$ catalysts for CO and CO_2 methanation. *Catal. Today* **2018**, *303*, 159–167. [CrossRef]
38. Beierlein, D.; Häussermann, D.; Pfeifer, M.; Schwarz, T.; Stöwe, K.; Traa, Y.; Klemm, E. Is the CO_2 methanation on highly loaded $Ni\text{-}Al_2O_3$ catalysts really structure-sensitive? *Appl. Catal. B Environ.* **2019**, *247*, 200–219. [CrossRef]
39. Zeng, L.; Weber, A.P. Aerosol synthesis of nanoporous silica particles with controlled pore size distribution. *J. Aerosol Sci.* **2014**, *76*, 1–12. [CrossRef]
40. Okuyama, K.; Wuled Lenggoro, I. Preparation of nanoparticles via spray route. *Chem. Eng. Sci.* **2003**, *58*, 537–547. [CrossRef]
41. Röhrbein, J.; Arias, A.M.; Weber, A.P. Aerosol-Synthese von porösen Katalysatorpartikeln mit einstellbaren Porengrößen und Katalysatordurchmessern. *Chem. Ing. Tech.* **2017**, *89*, 1739–1751. [CrossRef]
42. Khodakov, A.Y.; Griboval-Constant, A.; Bechara, R.; Zholobenko, V.L. Pore Size Effects in Fischer Tropsch Synthesis over Cobalt-Supported Mesoporous Silicas. *J. Catal.* **2002**, *206*, 230–241. [CrossRef]
43. Shannon, R.D. Revised effective ionic radii and systematic studies of interatomic distances in halides and chalcogenides. *Acta Crystallogr. Sect. A* **1976**, *32*, 751–767. [CrossRef]
44. St. O'Neill, H.C.; Dollase, W.A.; Ross, C.R. Temperature dependence of the cation distribution in nickel aluminate ($NiAl_2O_4$) spinel: A powder XRD study. *Phys. Chem. Miner.* **1991**, *18*, 302–319. [CrossRef]
45. Zhou, R.S.; Snyder, R.L. Structures and transformation mechanisms of the η, γand θtransition aluminas. *Acta Crystallogr. Sect. B Struct. Sci.* **1991**, *47*, 617–630. [CrossRef]
46. Cao, A.; Lu, R.; Veser, G. Stabilizing metal nanoparticles for heterogeneous catalysis. *Phys. Chem. Chem. Phys. PCCP* **2010**, *12*, 13499–13510. [CrossRef]
47. Hansen, T.W.; Delariva, A.T.; Challa, S.R.; Datye, A.K. Sintering of catalytic nanoparticles: Particle migration or Ostwald ripening? *Accounts Chem. Res.* **2013**, *46*, 1720–1730. [CrossRef]
48. Cao, A.; Veser, G. Exceptional high-temperature stability through distillation-like self-stabilization in bimetallic nanoparticles. *Nat. Mater.* **2010**, *9*, 75–81. [CrossRef]
49. Petroski, J.M.; Wang, Z.L.; Green, T.C.; El-Sayed, M.A. Kinetically Controlled Growth and Shape Formation Mechanism of Platinum Nanoparticles. *J. Phys. Chem. B* **1998**, *102*, 3316–3320. [CrossRef]
50. van de Loosdrecht, J.; van der Kraan, A.M.; van Dillen, A.J.; Geus, J.W. Metal-Support Interaction: Titania-Supported and Silica-Supported Nickel Catalysts. *J. Catal.* **1997**, *170*, 217–226. [CrossRef]
51. Zoz, W.; Gonzalez, R. Stabilization and sintering of porous Pt/SiO_2: A new approach. *Appl. Catal. A Gen.* **1993**, *102*, 181–200. [CrossRef]
52. Khodakov, A.Y. Enhancing cobalt dispersion in supported Fischer-Tropsch catalysts via controlled decomposition of cobalt precursors. *Braz. J. Phys.* **2009**, *39*, 171–175. [CrossRef]

53. Friedland, J.; Kreitz, B.; Grimm, H.; Turek, T.; Güttel, R. Measuring Adsorption Capacity of Supported Catalysts with a Novel Quasi-Continuous Pulse Chemisorption Method. *ChemCatChem* **2020**, *12*, 4373–4386. [CrossRef]
54. Mile, B.; Stirling, D.; Zammitt, M.A.; Lovell, A.; Webb, M. The location of nickel oxide and nickel in silica-supported catalysts: Two forms of "NiO" and the assignment of temperature-programmed reduction profiles. *J. Catal.* **1988**, *114*, 217–229. [CrossRef]
55. Burattin, P.; Che, M.; Louis, C. Metal Particle Size in Ni/SiO_2 Materials Prepared by Deposition-Precipitation: Influence of the Nature of the Ni(II) Phase and of Its Interaction with the Support. *J. Phys. Chem. B* **1999**, *103*, 6171–6178. [CrossRef]
56. Zieliński, J. Reductibility of silica supported nickel oxide. *Catal. Lett.* **1995**, *31*, 47–56. [CrossRef]
57. Ho, S.C.; Chou, T.C. The Role of Anion in the Preparation of Nickel Catalyst Detected by TPR and FTIR Spectra. *Ind. Eng. Chem. Res.* **1995**, *34*, 2279–2284. [CrossRef]
58. Louis, C.; Cheng, Z.X.; Che, M. Characterization of nickel/silica catalysts during impregnation and further thermal activation treatment leading to metal particles. *J. Phys. Chem.* **1993**, *97*, 5703–5712. [CrossRef]
59. Zhang, L.; Lin, J.; Chen, Y.W. Studies of Surface NiO Species in NiO/SiO_2 Catalysts using Temperature-programmed Reduction and X-Ray Diffraction. *J. Chem. Soc. Faraday Trans. 1 Phys. Chem. Condens. Phases* **1992**, *88*, 2075–2078. [CrossRef]
60. Burattin, P.; Che, M.; Louis, C. Ni/SiO_2 Materials Prepared by Deposition-Precipitation: Influence of the Reduction Conditions and Mechanism of Formation of Metal Particles. *J. Phys. Chem. B* **2000**, *104*, 10482–10489. [CrossRef]
61. Coenen, J.W. Characterization of the standard nickel/silica catalyst EuroNi-1. *Appl. Catal.* **1989**, *54*, 65–78. [CrossRef]
62. Bartholomew, C.H. Chemistry of Nickel-Alumina Catalysts. *J. Catal.* **1976**, *45*, 41–53. [CrossRef]
63. Ewald, S.; Hinrichsen, O. On the interaction of CO_2 with Ni-Al catalysts. *Appl. Catal. A Gen.* **2019**, *580*, 71–80. [CrossRef]
64. Goodwin, D.G.; Speth, R.L.; Moffat, H.K.; Weber, B.W. Cantera: An Object-oriented Software Toolkit for Chemical Kinetics, Thermodynamics, and Transport Processes. Version 2.4.0. 2018. Available online: https://www.cantera.org (accessed on 24 August 2020).
65. Rusic, B.; Bross, D.H. Active Thermochemical Tables (ATcT) Values Based on ver. 1.122g of the Thermochemical Network (2019). Available online: https://atct.anl.gov/ (accessed on 7 August 2020).
66. Burcat, A.; Ruscic, B. *Third Millenium Ideal Gas and Condensed Phase Thermochemical Database for Combustion (with Update from Active Thermochemical Tables)*; Technical Report; Argonne National Lab.(ANL): Argonne, IL, USA, 2005.
67. Bjørgum, E.; Chen, D.; Bakken, M.G.; Christensen, K.O.; Holmen, A.; Lytken, O.; Chorkendorff, I. Energetic mapping of Ni catalysts by detailed kinetic modeling. *J. Phys. Chem. B* **2005**, *109*, 2360–2370. [CrossRef]
68. Weatherbee, G.D.; Bartholomew, C.H. Hydrogenation of CO_2 on Group VIII Metal: I. Specific Activity of Ni/SiO_2. *J. Catal.* **1981**, *68*, 67–76. [CrossRef]
69. Karam, L.; Reboul, J.; El Hassan, N.; Nelayah, J.; Massiani, P. Nanostructured Nickel Aluminate as a Key Intermediate for the Production of Highly Dispersed and Stable Nickel Nanoparticles Supported within Mesoporous Alumina for Dry Reforming of Methane. *Molecules* **2019**, *24*, 4170. [CrossRef]
70. Aziz, M.; Jalil, A.A.; Triwahyono, S.; Saad, M. CO_2 methanation over Ni-promoted mesostructured silica nanoparticles: Influence of Ni loading and water vapor on activity and response surface methodology studies. *Chem. Eng. J.* **2015**, *260*, 757–764. [CrossRef]
71. Vrijburg, W.L.; van Helden, J.W.A.; van Hoof, A.J.F.; Friedrich, H.; Groeneveld, E.; Pidko, E.A.; Hensen, E.J.M. Tunable colloidal Ni nanoparticles confined and redistributed in mesoporous silica for CO_2 methanation. *Catal. Sci. Technol.* **2019**, *9*, 2578–2591. [CrossRef]
72. Ren, J.; Guo, H.; Yang, J.; Qin, Z.; Lin, J.; Li, Z. Insights into the mechanisms of CO_2 methanation on Ni(111) surfaces by density functional theory. *Appl. Surf. Sci.* **2015**, *351*, 504–516. [CrossRef]
73. Vogt, C.; Groeneveld, E.; Kamsma, G.; Nachtegaal, M.; Lu, L.; Kiely, C.J.; Berben, P.H.; Meirer, F.; Weckhuysen, B.M. Unravelling structure sensitivity in CO_2 hydrogenation over nickel. *Nat. Catal.* **2018**, *1*, 127–134. [CrossRef]
74. Blaylock, D.W.; Zhu, Y.A.; Green, W.H. Computational Investigation of the Thermochemistry and Kinetics of Steam Methane Reforming Over a Multi-Faceted Nickel Catalyst. *Top. Catal.* **2011**, *54*, 828–844. [CrossRef]

75. Weber, A.P.; Seipenbusch, M.; Kasper, G. Size Effects in the Catalytic Activity of Unsupported Metallic Nanoparticles. *J. Nanoparticle Res.* **2003**, *5*, 293–298. [CrossRef]
76. Ertl, G.; Knözinger, H.; Schüth, F.; Weitkamp, J. *Handbook of Heterogeneous Catalysis*; Wiley-VCH Verlag GmbH & Co. KGaA: Weinheim, Germany, 2008. [CrossRef]